Computers and Fluids 266 (2023) 106058

Contents lists available at ScienceDirect

Computers and Fluids

journal homepage: www.elsevier.com/locate/compfluid

On the coupling between wall-modeled LES and immersed boundary method towards applicative compressible flow simulations

Francesco De Vanna [a,*], Giacomo Baldan [b], Francesco Picano [a,c], Ernesto Benini [a]

[a] Department of Industrial Engineering, Università degli Studi di Padova, Via Venezia 1, Padova 35131, Italy
[b] Department of Aerospace Science and Technology, Politecnico di Milano, Via La Masa 34, Milano 20156, Italy
[c] Centro di Ateneo di Studi e Attività Spaziali "Giuseppe Colombo" (CISAS), Università degli Studi di Padova, Via Venezia 15, Padova 35131, Italy

ARTICLE INFO

Keywords:
Large-eddy simulation
Wall-modeling
Immersed boundary method
Compressible flows
Engineering flows
Graphic processing units

ABSTRACT

The current work presents an innovative numerical technique for high-Reynolds/high-Mach number compressible flow simulations in complex configurations. In particular, the research combines a novel wall-modeled large-eddy simulation technique with a sharp-interface immersed boundary method in the framework of high-order numerical schemes. The proposed approach enables the best from wall modeling and the immersed boundary. The first is concerned with accurately dealing with wall flows while avoiding direct control of near-wall resolution; the second is related to efficiently treating arbitrarily complex geometries in Cartesian grids. In particular, the paper extends a well-established wall model already presented by the research group to arbitrarily-shaped bounds. The method yields a minimally invasive technique that switches between wall-resolved and wall-modeled large-eddy simulations according to the local near-wall resolution. Thus, easily fitting aerodynamic simulation needs. After discussing the numerical procedure, the paper provides several benchmarks to demonstrate the validity of the proposed approach. In particular, literature-available direct numerical datasets are mined to compare acquired outcomes. The results' accuracy is found to be remarkable from low-Mach-channel and -pipe flow configurations up highly-compressible flows concerning the spatial deployment of the boundary layer over a flat plate and the shock-wave/boundary-layer interaction over a compression ramp. Thus, the proposed method appears to be a promising framework for dealing with engineering-relevant flow simulations along with the efficient path of Cartesian meshes combined with massively parallel GPU-accelerated architectures.

1. Introduction

Nowadays, Computational Fluid Dynamic (CFD) is a state-of-the-art tool in industry and research to solve problems involving the evolution of flows over increasingly complex geometries. Latest technological improvements in computing architectures, in fact, have made it possible to significantly alter the design processes in several industrial sectors – primarily aerospace and energy – by virtually prototyping a broad spectrum of engineering machines thanks to enhanced fluid dynamics simulations. As a result, CFD has lowered testing requirements and has been able to provide answers to crucial physical questions that might restrict design performance.

However, advanced engineering applications require high-fidelity CFD models to create prototypes that closely mimic real-world operational devices. Therefore, in this regard, scale-resolved CFD methodologies like Direct Numerical Simulations (DNSs) or Large-Eddy Simulations (LESs) are getting increasing attention from research centers and advanced engineering sectors as they represent the most reliable approaches for addressing time-dependent and complex-flow problems. However, it is worth noting that DNSs or LESs procedures often do not suit the availability of industrial computer resources. The first approach, DNSs, in fact, aiming to resolve the entire turbulent spectrum, results in the need for very dense grids, thus applying only to academic configurations. On the other hand, LESs, even leveraging on Kolmogorov's theory and aiming at modeling the universal SubGrid-Scale (SGS) turbulent structures, fail immediately in near-wall situations due to non-homogeneity of turbulence near the walls, therefore, requiring resolution roughly similar to DNS in applicative wall flows arrangements. Chapman [1] and Choi and Moin [2] demonstrated that the number of grid points required to resolve near-wall eddies for DNS and Wall-Resolved LES (WRLES), i.e., an LES strategy in which the boundary layer is fully resolved, is approximative $N_{DNS} \sim Re^{37/14}$ and $N_{WRLES} \sim Re^{13/7}$, where Re is the Reynolds number based on a characteristic length of the problem. Taking a practical

* Corresponding author.
E-mail address: francesco.devanna@unipd.it (F. De Vanna).

https://doi.org/10.1016/j.compfluid.2023.106058
Received 13 May 2023; Received in revised form 26 July 2023; Accepted 14 September 2023
Available online 19 September 2023

example, if we aim to analyze the aerodynamics performance of a standard airplane/gas turbine airfoil with a chord Reynolds number of $Re_c \approx 10^7$ we get that a DNS requires $N_{DNS} \approx 10^{18}$ points, while a WRLES is around approximately $N_{WRLES} \approx 10^{13}$ points. Consequently, Reynolds-Averaged Navier–Stokes (RANS) techniques, which model the entire turbulent spectrum, remain the most commonly used approach in the industry despite their limited predictive capacity, especially in time-dependent flow configurations. A reasonable compromise to deal with time-varying turbulent flows in aerodynamic applications seems to adopt a LES framework in which the near-wall portions are handled with some reduced-order model. Such hybrid approaches, in fact, will retain modeling the multi-scalar nature of the flow, keeping the computational costs affordable. Along this thread, the development of increasingly complex hybrid RANS/LES algorithms has succeeded considerably [3], and, in this framework, the so-called Wall-Modeled LES (WMLES), i.e., an LES strategy in which the outer-layer eddies and energy-carrying turbulent structures are resolved while the near-wall regions are modeled, take place [4]. Compared to other hybrid/zonal numerical discretizations of the Navier–Stokes equations, the WMLES approach has been demonstrated to be more accurate in capturing dynamical effects in the boundary layer, a crucial requirement for accurate prediction of compressible flows [5]. Following this path, several contributions to the WMLES paradigm have appeared recently [6–16] and the reader is addressed to recent reviews by Larsson et al. [17] and Bose and Park [5] for a comprehensive description of the method. The point we want to stress here is that – still according to Chapman [1] and Choi and Moin [2] – WMLES scales linearly with the Reynolds number, i.e., $N_{WMLES} \sim Re$; thus, certainly making such a strategy more expensive than RANS but affordable at the industrial level without resorting to particularly advanced computing facilities.

The challenge of turbulence modeling is not the sole factor influencing high-Reynolds number simulations in applications. Efficiently processing complex geometries, in fact, is not effortless. In this path, the Immersed Boundary Method (IBM) can represent a straightforward solution. The approach enables the simulation of arbitrarily-shaped geometries within fully-structured Cartesian grids. Compared to other strategies aiming at treating complex geometries (e.g., body-fitted-grid methods), the IBM primarily provides the following benefits: (i) in compressible conditions, it can be rendered with fully explicit algorithms; (ii) it is minimally invasive if coupled with existing DNS/LES solvers; (iii) it is unbeatable in scaling performance when combined with massive-parallel architectures, especially those adopting modern Graphics Processing Units (GPUs). Such peculiarities made IBM a popular choice for a broad range of applications and several scientists adopted the method in recent years. In particular, from the original biological-related work by Peskin [18], IB formulations have spread in literature collecting a wide variety of flow problems of very different nature [19–38]. The interested reader is referred to Verzicco [39] for a freshly published review about the method. Compared to body-fitted strategies, what is detrimental to IBM is the lack of direct control of the boundary layer resolution.

This is the source of inspiration for the present work. The combination of WMLES, which aims to place the first off-the-wall point as far as possible from the boundary surface without any direct control of the near-wall resolution, and the IBM appears very promising for dealing with arbitrarily-shaped aerodynamics applications with a marked integration on GPU-enabled solvers. Thus, the current study proposes a novel numerical approach that combines the WMLES strategy with IBM to handle CFD simulations of complex geometries in high-Reynolds/high-Mach conditions. Here we cannot fail to mention that the idea of combining the IBM with wall-modeling is not entirely new in the literature. Cristallo and Verzicco [40], for instance, proposed a slip-velocity boundary condition based on the boundary layer equilibrium equation for the tangential velocity components. Roman et al. [41], advanced a wall-layer which assumed the logarithmic law behavior for point used in the immersed boundary extrapolation process. Tamaki and Kawai [42] proposed a partial-slip wall-boundary condition for obtaining the logarithmic law of the wall for the mean streamwise velocity on non-body-conforming grids by also accounting corrections to minimizes the adverse effects on the resolved turbulence. However, compared to already available and similar methods, the present strategy provides peculiar features. In particular: (i) the wall model is arranged so that the wall-shear stress and the heat flux are enforced at the boundary surface by augmenting the turbulent viscosity and diffusivity and preserving the no-slip and the isothermal/adiabatic conditions. To the authors' best knowledge, such a strategy has never been addressed in compressible conditions and partially explored in incompressible frameworks [43,44]; (ii) the method, by generalizing the unified WR/WMLES approach by De Vanna et al. [45], reverts to a standard wall-resolved-type boundary treatment if the local resolution allows it by smoothly and dynamically transit between WRLES and WMLES, a property that fits very well the complex dynamics of the boundary layer over non-conformal geometries; (iii) because of its whole explicitness, the method is minimal invasive concerning existing DNS/LES solvers and easily coupled with parallel algorithms in multi-GPU logic.

Model validation is provided over four increasingly complex arrangements. In particular, as a first step, a low-Mach channel flow configuration is adopted as the baseline case, the latter representing an incompressible in-equilibrium flow on conformal walls. Then, we move on to a pipe flow setup, still a low-Mach in-equilibrium setup, but with the non-trivial challenge of the non-conformal wall arrangement. As a third scenario, a compressible boundary layer is examined that poses complexity about the high-Mach conditions while keeping the geometry conformal to the grid. All these configurations are also motivated since they provide a wealth of DNS literature comparisons which can be used to assess the efficacy of the proposed technique. Nevertheless, they are all revisited in IBM logic by considering the walls as submerged solids in conjunction with the generalized WMLES strategy rather than taking them as limit bounds, as is customary for such canonical analysis. Finally, since the suggested technique is aimed at complex geometries, the paper closes with a description and analysis of compressible flow aerodynamics through a compression ramp configuration. Such a test case exposes all of the proposed method's complexities in terms of non-conformal bounds, compressible features, and turbulence modeling, demonstrating how the proposed technique can represent a feasible alternative in the aerodynamic characterization of complex geometries in all application sectors where high-Mach and high-Reynolds numbers control the flow characteristics.

The following is a breakdown of the present document organization: Sections 2 and 3 provide the essential information concerning the numerical model and numerical methods, respectively. Section 4 presents the results of the analyses, while Section 5 states the conclusions and the final remarks.

2. Solver structure

2.1. Governing equations

Present computations are made using URANOS (Unsteady Robust All-around Navier–StOkes Solver). The solver is a well-established GPU-enabled code developed at the Industrial Engineering Department of the University of Padova [46] and now distributed under BSD Licence 2.0here[1]. URANOS, in particular, deals with the filtered compressible Navier–Stokes system of equations in a conservative formulation and,

[1] URANOS: https://gitlab.com/fralusa/uranos_gpu

in particular, the Reynolds ($\phi = \bar{\phi} + \phi'$) and the Favre ($\phi = \tilde{\phi} + \phi''$, $\tilde{\phi} = \overline{\rho\phi}/\bar{\rho}$) decompositions are used. The model reads as:

$$\frac{\partial \bar{\rho}}{\partial t} + \frac{\partial \bar{\rho}\tilde{u}_j}{\partial x_j} = 0 \tag{1a}$$

$$\frac{\partial \bar{\rho}\tilde{u}_i}{\partial t} + \frac{\partial \bar{\rho}\tilde{u}_i\tilde{u}_j}{\partial x_j} = -\frac{\partial \bar{p}\delta_{ij}}{\partial x_j} + \frac{\partial \bar{\tau}_{ij}}{\partial x_j} - \frac{\partial T_{ij}^{SGS}}{\partial x_j} + f_i \tag{1b}$$

$$\frac{\partial \bar{\rho}\tilde{E}}{\partial t} + \frac{\partial \bar{\rho}\tilde{u}_j\tilde{E}}{\partial x_j} = -\frac{\partial \bar{p}\tilde{u}_j}{\partial x_j} + \frac{\tilde{u}_j\bar{\tau}_{ij}}{\partial x_j} - \frac{\partial \bar{J}_j}{\partial x_j} - \frac{\partial E_j^{SGS}}{\partial x_j} + f_i\tilde{u}_i \tag{1c}$$

Here $\bar{\rho}$ is the filtered density, $\tilde{u}_i$ is the filtered velocity component along with the ith direction, $\bar{p}$ is the filtered thermodynamic pressure, $\tilde{E} = \tilde{e} + \widetilde{u_i u_i}/2$ is the filtered total energy per unit mass, $\tilde{e}$ is the filtered internal energy per unit mass and $\bar{J}_j$ is the jth component of the filtered molecular heat flux. The above system equations is closed by the ideal gas equation of state, $\bar{p} = \bar{\rho}R\tilde{T}$, and a constitutive expression for the internal energy, $\tilde{e} = c_v\tilde{T}$. Here $\tilde{T}$ denotes the filtered temperature, R is the specific gas constant, $c_v = R/(\gamma - 1)$ and $c_p = \gamma R/(\gamma - 1)$ are the specific heat at constant volume and pressure, respectively, while $\gamma = c_p/c_v$ is specific heat ratio. The viscous stress tensor, $\bar{\tau}_{ij}$, and heat flux components, $\bar{J}_j$, are accounted as following:

$$\bar{\tau}_{ij} = 2\mu(\tilde{T})\left(\tilde{S}_{ij} - \frac{1}{3}\tilde{S}_{kk}\delta_{ij}\right) \tag{2}$$

$$\bar{J}_j = -\lambda(\tilde{T})\frac{\partial \tilde{T}}{\partial x_j} \tag{3}$$

where $\mu(\tilde{T})$ is the molecular viscosity, $\lambda(\tilde{T}) = c_p\mu(\tilde{T})/Pr$ is the thermal diffusivity and $\tilde{S}_{ij} = {}^1/_2\left(\tilde{g}_{ij} + \tilde{g}_{ji}\right)$ denotes the filtered resolved strain-rate tensor with $\tilde{g}_{ij} = \partial\tilde{u}_i/\partial x_j$ the filtered resolved velocity gradient. The molecular viscosity, $\mu(\tilde{T})$, is modeled through the Sutherland's two coefficients law

$$\bar{\mu}(\tilde{T}) = \tilde{T}^{3/2}\left(\frac{T_0 + S}{\tilde{T} + S}\right) \tag{4}$$

where T_0 and $S = 110.4$K denote the reference temperature and Sutherland's empirical parameter, respectively. The model is made non-dimensional so that the system conditions can be established unambiguously by varying γ, Pr, Re, and Ma. As a standard rule, γ and Pr are set to 1.4 and 0.71, respectively. Finally, the forcing term, f_i, is introduced to discretely enforce constant mass-flow-rate in time to cope with channel and pipe flow simulations. The matching power, $f_i\tilde{u}_i$, is likewise added to the total energy equation's right side.

2.2. Turbulence modeling

The SubGrid Scale (SGS) stress tensor, $T_{ij}^{SGS} = \overline{\rho u_i u_j} - \bar{\rho}\tilde{u}_i\tilde{u}_j$, is accounted via the Boussinesq's hypothesis

$$T_{ij}^{SGS} - \frac{1}{3}T_{kk}^{SGS}\delta_{ij} = -2\mu_{SGS}\left(\tilde{S}_{ij} - \frac{1}{3}\tilde{S}_{kk}\delta_{ij}\right) \tag{5}$$

where μ_{SGS} is the SGS viscosity and T_{kk}^{SGS} is the isotropic contribution. According to Garnier et al. [47], T_{kk}^{SGS} is neglected since it is non-negligible only near shocks where the numerical schemes inject a significant amount of artificial dissipation. SGS terms in the energy equation are given by

$$E_j^{SGS} = \overline{(\rho E + p)u_j} - (\bar{\rho}\tilde{E} + \bar{p})\tilde{u}_j = \tag{6a}$$

$$= \underbrace{\left[\overline{\rho c_p T u_j} - \bar{\rho}c_p\tilde{T}\tilde{u}_j\right]}_{\mathcal{Q}_j} + \underbrace{\left[\frac{1}{2}\overline{(\rho u_i u_i u_j} - \bar{\rho}\tilde{u}_i\tilde{u}_i\tilde{u}_j)\right]}_{\psi_{iij}} - \frac{1}{2}T_{ii}^{SGS}\tilde{u}_j \tag{6b}$$

where $\mathcal{Q}_j = -\lambda_{SGS}\partial\tilde{T}/\partial x_j$ denotes the SGS heat flux, with $\lambda_{SGS} = c_p\mu_{SGS}/Pr_{SGS}$, and ψ_{iij} is the velocity triple correlation tensor whose contribution is neglected. Pr_{SGS}, the SGS Prandtl number, is assumed equal to 0.9.

In the present work, the Wall-Adaptive Large-Eddy (WALE) model by Nicoud and Ducros [48] is used to account for the SGS viscosity. The model reads as follows:

$$\mu_{SGS} = \bar{\rho}(C_w\Delta)^2\frac{(S_{ij}^d S_{ij}^d)^{3/2}}{(S_{ij}S_{ij})^{5/2} + (S_{ij}^d S_{ij}^d)^{5/4}} \tag{7}$$

Here S_{ij}^d denotes the traceless symmetric part of the square of the resolved velocity gradient, i.e.,

$$S_{ij}^d = \frac{1}{2}\left(\tilde{g}_{il}\tilde{g}_{lj} + \tilde{g}_{jl}\tilde{g}_{li}\right) - \frac{1}{3}\tilde{g}_{ml}\tilde{g}_{lm}\delta_{ij} \tag{8}$$

and $\tilde{g}_{ij}$ still represents the resolved velocity gradient. $C_w = 0.325$ is the model constant while $\Delta = (\Delta x_1\Delta x_2\Delta x_3)^{1/3}$ is the local mesh size. Among the several algebraic eddy viscosity formulations, the WALE model has unique qualities that are very useful when paired with embedded geometries. The model, in fact, automatically delivers the right eddy viscosity behavior in near-wall areas without requiring any dumping function or transition between the bulk flow and the boundary layer by providing the $\mu_{SGS}/\mu \sim \mathcal{O}(y^+)^3$ asymptotic behavior at the wall locations [49]. The research group has already successfully employed such a modeling framework for aerodynamics applications, and the reader can look at De Vanna et al. [37],De Vanna et al. [38] for some examples.

2.3. Immersed boundary method

Complex geometries are treated with the sharp-interface IBM by De Vanna et al. [36]. A quick summary of the method is given here from a theoretical perspective, while later in this paper, the numerical aspects are provided. In particular, URANOS handles two-dimensional sketches associated with immersed objects by the `.msh` file format. With this framework, each immersed body, $b = 1, \dots, N$, is represented by a set of closed points $\{\mathbf{x}_l^b\}_{l=1}^n$ and edges $\{e_l^b\}_{l=1}^{n-1}$ on a Cartesian mesh. As a result, after the entire set of many-edged polygons is obtained, each Cartesian grid point is flagged whether it is within or outside the polygon. The process follows a classical ray-tracing algorithm according to o'Rourke [50], and it is managed as a pre-processing activity. Thus, being D the whole computational domain, this is divided into three portions: Ω_s, Ω_f, and Ω_g, the latter being the solid, the fluid, and ghost domain regions, respectively. The information is stored in a marker variable. It is essential to highlight that $\Omega_s \cup \Omega_f = D$. Thus, the ghost region is a function of both the solid and fluid portions. The latter, in particular, is defined as follow

$$\Omega_g = \{(x_i, y_j, z_k) \in \Omega_s \text{ if } \exists (x_l, y_m, z_n) \in \Omega_f \text{ for } (l, m, n) = (i, j, k) - ng, \dots, (i, j, k) + ng\} \tag{9}$$

and consists of ng layers of points that are required for the high-order numerical scheme stencils discretization. Such a data structure allows using the ghost nodes, i.e., $\mathbf{x}_g$ such that $(x_i, y_j, z_k) \in \Omega_g$, to prescribe any boundary condition through an arbitrary complex surface. In particular, in the case of fully resolved wall regions, just the primitive (i.e., $\tilde{u}, \tilde{v}, i\tilde{w}, \bar{p}, \tilde{T}$), and consequently the conserved (i.e., $\bar{\rho}$, $\bar{\rho}\tilde{u}$, $\bar{\rho}\tilde{v}$, $\bar{\rho}i\tilde{w}$, $\bar{\rho}\tilde{E}$) variables, are forced in Ω_g to prescribe the desired boundary condition. Conversely, if the wall is not sufficiently resolved, the WMLES strategy is included in the wall treatment by using the ghost nodes to prescribe the correct wall-shear stress and heat flux. The numerical procedure underlying the IB approach in wall-resolved arrangements is amply detailed in Ref. [36], while, in the present work, a clear description of the method, if combined with the wall model, is provided in Section 3.

2.4. Near wall treatment

In the case of poorly resolved wall regions, URANOS uses a WM-LES framework. The current code version, in particular, caters to an equilibrium-based wall model that implies the instantaneous balancing

between convection terms and the pressure gradient. As a result, two unknowns emerge, U_{wm} and T_{wm}, which reflect the mean wall parallel speed and temperature distribution, respectively. The subscript wm indicates that these values are computed by solving the wall model rather than the classical Navier–Stokes equations that compete with the LES solver. In particular, according to the thin boundary layer hypothesis, the near-wall Navier–Stokes system of equations along with the wall-normal direction, here denoted with y, simplifies to:

$$\frac{d}{dy}\left(\mu_{wm}^{tot}\frac{dU_{wm}}{dy}\right)=0 \tag{10a}$$

$$\frac{d}{dy}\left(\lambda_{wm}^{tot}\frac{dT_{wm}}{dn}\right)=-\frac{d}{dy}\left(\mu_{wm}^{tot}U_{wm}\frac{dU_{wm}}{dy}\right) \tag{10b}$$

where

$$\mu_{wm}^{tot}=\mu_{wm}+\mu_{t,wm} \tag{11a}$$

$$\lambda_{wm}^{tot}=\frac{c_p\mu_{wm}}{Pr}+\frac{c_p\mu_{t,wm}}{Pr_{t,wm}} \tag{11b}$$

are the overall model viscosity and thermal diffusivity, respectively, c_p is the specific heat at constant pressure, $Pr_{t,wm}=0.9$ denotes the turbulent Prandtl number, $\mu_{wm}=\mu_{wm}(T_{wm})$ is the molecular wall model viscosity, still assumed satisfying Sutherland's law, $\mu_{t,wm}=\kappa\rho_{wm}u_\tau yD$ is the wall model eddy viscosity and $\kappa=0.41$ is the Von Kármán constant. $\rho_{wm}=p^{LES}/(RT_{wm})$ is the wall model density distribution, p_{LES} is the external LES pressure, and $D=\left[1-\exp\left(-y^*/A^+\right)\right]^2$ is the Van Driest dumping function with $A^+=17$ and $y^*=y\sqrt{\rho_{wm}\tau_{w,wm}}/\mu_{wm}$ the model parameter and the wall-normal distance in semi-local scaling, respectively. Such a system of Ordinary Differential Equations (ODEs) is solved on a separate grid embedded in the LES main mesh. The grid for the wall model starts at each $y=0$ immersed wall location, where speed and temperature/temperature-gradient are known, and extends to an exchange site, $y=\hbar$, where the model meets the outer flow conditions

$$U_{wm}=u_{/\!/}^{LES},\quad T_{wm}=T^{LES},\quad P_{wm}=p^{LES} \tag{12}$$

being $u_{/\!/}^{LES}$, T^{LES}, and p^{LES}, the outer LES solution in terms of wall-parallel velocity, static temperature, and static pressure. After solving Eqs. (10), the U_{wm} and T_{wm} distributions are used to calculate the wall shear stress and heat flux. The information is then enforced as a boundary condition via the proposed IB strategy. The process's technical details for conformal walls are widely documented in Refs. [45,51,52] while Section 3 will provide the details about an arbitrarily-shaped surface.

3. Numerical methods

The Navier–Stokes system of equations is discretized using a high-order finite difference approach, and URANOS allows for both uniform and non-uniform structured Cartesian meshes discretizations. The following provides a brief overview of the adopted schemes and numerical approaches.

3.1. Convective terms discretization

Convective fluxes are treated using a mix of the central-like Energy-Preserving (EP) approach by Pirozzoli [53] and the low-dissipative Targeted Essentially Non-Oscillatory (TENO) strategy by Fu et al. [54,55,56].

Specifically, the sixth-order EP scheme is used, which aims to provide semi-discrete conservation of total kinetic energy in the limit of incompressible, inviscid flows and can be used in non-shocked configurations or flow smooth portions [57–59]. The framework enables a stable spatial treatment of convective contributions with theoretically zero numerical dissipation and increased stability compared to conventional central-like discretizations. By examining Modesti and Pirozzoli [60,61], the reader is pointed to a range of compelling applications where the EP scheme is adopted effectively.

On the other hand, high-order TENO methods are used to develop the flow's shocked/shocklet regions. Peculiarly, TENO methods introduce a discrete cut-off function that removes non-smooth candidate stencils in the flux reconstruction compared to a more conventional WENO implementation [62–64]. In addition, adaptive TENO versions are used, which embed a shock sensor to adjust the threshold of the C_T parameter in different regions of the domain to recover more stencils from the reconstruction in smooth regions [65,66]. The scheme's parameters are those suggested by Fu et al. [55,56].

3.2. Shock detection

In addition to the TENO adaptivity, shock-capturing is only activated when some flow requirements are met, leaving most of the domain to the computationally efficient EP scheme. Since, especially in low-resolution environments like one associated with WMLES, multiple zones of supposedly smooth flow are identified through ENO-like reconstructions, shock detection systems often misidentify spurious noise and oscillation as shocklets. Thus, the current study adopts a modified Ducros sensor that is found peculiarly accurate in such cases, with minimal intrusion of shock-capturing where it is not required [67,68]. The sensor reads as follows:

$$\theta=\max\left(-\frac{\partial\tilde{u}_i/\partial x_i}{\sqrt{(\partial\tilde{u}_i/\partial x_i)^2+(\epsilon_{ijk}\partial\tilde{u}_k/\partial x_j)^2+\epsilon_0^2}},0\right) \tag{13}$$

Here, ϵ_{ijk} is the Levi-Civita permutation tensor, whereas $\epsilon_0=u_\infty/L_0$ represents a reference velocity gradient. Thus, if the cell-bound sensor value, $\theta_{i+1/2}$, exceeds a precomputed threshold, $\bar{\theta}$, the flow is judged shocked, and the shock-capturing approach is adopted in the flagged cell and some surrounding cells whose number depends by the TENO order of accuracy. In contrast, the EP method is used.

3.3. Viscous terms discretization

Unique to URANOS is its ability to handle viscous fluxes using the semi-conservative finite-difference formulation by De Vanna et al. [69]. In the case of uniform flow properties, the method provides equivalent to central finite-difference derivatives approximations with the corresponding order of accuracy. In contrast, in variable viscosity/diffusion conditions, typical of LES/WMLES of compressible wall flows, the method provides strong preservation and accurate telescoping of viscous/diffusion terms. Present computations adopt the sixth-order version of the method.

3.4. Temporal integration

The solver core is completed by third-order low-storage total variation diminishing Runge–Kutta method by Gottlieb and Shu [70], the method being considered one of the best options for compressible flows temporal integration. Thus, being $\mathcal{N}(\mathbf{U})$ a high-order numerical representation of the non-linear spatial differential operators applied to the conserved variables, $\mathbf{U}=\{\bar{\rho},\bar{\rho}\tilde{u}_i,\bar{\rho}\tilde{E}_{tot}\}^T$, the method reads as:

$$\mathbf{U}^{(1)}=\mathbf{U}^n+\Delta t\mathcal{N}(\mathbf{U}^n) \tag{14a}$$

$$\mathbf{U}^{(2)}=\frac{3}{4}\mathbf{U}^n+\frac{1}{4}\mathbf{U}^{(1)}+\frac{1}{4}\Delta t\mathcal{N}(\mathbf{U}^{(1)}) \tag{14b}$$

$$\mathbf{U}^{(n+1)}=\frac{1}{3}\mathbf{U}^n+\frac{2}{3}\mathbf{U}^{(2)}+\frac{2}{3}\Delta t\mathcal{N}(\mathbf{U}^{(2)}) \tag{14c}$$

The time step is dynamically adjusted at each iteration to guarantee the simulation's stability. Each time step involves a dynamic computation and comparison of the Courant–Friedrichs–Lewy and Fourier criteria, with CFL and FO set to $CFL=0.5$ and $FO=0.1$, respectively. The least achievable time step between the two criteria is employed to advance the solution.

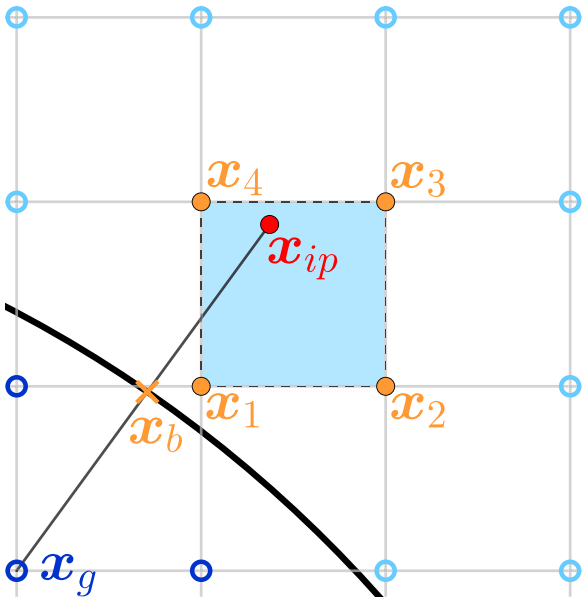

Fig. 1. Sketch of the immersed boundary interpolation procedure.

3.5. Numerical treatment of immersed walls

Fig. 1 is a graphical representation of the IBM adopted in present computations. Here $\mathbf{x}_g \in \Omega_g$ denotes a ghost point while $\mathbf{x}_{ip} \in \Omega_f$ represents its corresponding image point. As shown in the sketch, for each ghost point, a normal-to-bound probe is built, the latter crossing the boundary surface at the $\mathbf{x}_b$ location. The current strategy aims to interpolate the flow variables at the $\mathbf{x}_{ip}$ location to prescribe the desired boundary conditions and/or the proper wall-shear-stress/heat-flux. Interpolations assume that every flow variable behaves bilinearly at the subgrid level, i.e.,

$$\phi(x,y) = c_1 xy + c_2 x + c_3 y + c_4 \tag{15}$$

with $\{c_i\}_{i=1}^4$ being the interpolation coefficients to be determined.

A few exceptions must be mentioned from the numerical treatment sketched in Fig. 1. In particular, *(i)* The interpolation support, consisting of the points surrounding $\mathbf{x}_{ip}$, may include the ghost area with consequent issues in mass/momentum/energy conservation due to inappropriate boundary specifications; *(ii)* normal probes cannot be established near corners surfaces. In these two circumstances, the interpolation strategy takes a different route, the explanation of whom is not the primary aim of the present paper. Thus, the reader can fix the standard process in mind, as described in Fig. 1, while details on the present IBM are widely provided by De Vanna et al. [36].

Once an arbitrary flow variable, ϕ, is interpolated around the $\mathbf{x}_{ip}$ location, a no-slip wall condition is enforced by prescribing the value of ϕ in the corresponding ghost point, ϕ_g. In particular, if ϕ is subjected to a Dirichlet-type boundary condition, being ϕ_b the desired value of ϕ at the bound, ϕ_g is assigned as follows:

$$\phi_g = 2\phi_b - \phi_{ip}. \tag{16}$$

For Neumann-type boundaries, instead, ϕ_g reads as

$$\phi_g = \phi_{ip} \tag{17}$$

Following the suggestion by Piquet et al. [32], primitives variables, i.e., u, v, w, p and T, are used to enforce the boundary condition. Thus, for an adiabatic no-slip wall, Eq. (16) is applied to all velocity components, and Eq. (17) is used to prescribe a zero-gradient condition for the temperature and the pressure field, respectively. For an isothermal no-slip wall conditions, instead, wall temperature is imposed via Eq. (16) while velocity and pressure fields keep the same track as in adiabatic cases. Thus, the following expressions hold:

$$u_g = -u_{ip}, \quad v_g = -v_{ip}, \quad w_g = -w_{ip} \tag{18a}$$

$$T_g = 2\alpha T_b + \beta T_{ip} \tag{18b}$$

$$p_g = p_{ip} \tag{18c}$$

being $\alpha = 0$ and $\beta = 1$ for adiabatic arrangements, while $\alpha = 1$ and $\beta = -1$ for isothermal cases, respectively. This strategy can readily enforce the no-slip adiabatic/isothermal conditions to arbitrary-shaped bounds. However, second-order numerical treatment of near-wall quantities renders this approach effective if the boundary surface is sufficiently resolved. In high-Reynolds conditions, this is the primary limitation of the IBM. In fact, the image point may be quite far from the solid surface relative to the viscous unit, resulting in an underestimation of friction and wall heat flux. That is why the wall model takes charge. In such instances, the near-wall treatment allows us to prescribe the correct shear stress and heat flux values without resorting to excessive near-wall resolutions. The image point can be used as the initial location of the interface between the external LES solver and the near-wall region where the system described by Eqs. (10) is solved. Here is the step-by-step algorithm:

1. As a first step, the flow field is interpolated around the image point, $\mathbf{x}_{ip}$, according to Eq. (15). Thus, velocity components, $\tilde{u}_{ip}, \tilde{v}_{ip}, \tilde{w}_{ip}$, and overall viscosity and diffusivity values, μ_{ip}^{tot}, λ_{ip}^{tot}, are gathered.
2. Such values are used to compute a first guess of the wall parallel speed according to the following expression:

$$\tilde{u}_{/\!/}^* = \sqrt{(\tilde{u}_{ip} t_1 + \tilde{v}_{ip} t_2)^2 + \tilde{w}_{ip}^2} \tag{19}$$

   Here t_1 and t_2 denote the tangent versor components associated with the $\mathbf{x}_b$ location.
3. A first guess of the wall-shear stress, $\tau_w^* = \sqrt{u_\tau^*/\rho_w}$, is computed by iteratively solving Reichardt's law [71] in terms of u_τ^*:

$$\frac{\tilde{u}_{/\!/}^*}{u_\tau^*} = \kappa^{-1}\log\left(1+\kappa y^+\right) + 7.8\left(1 - e^{-\frac{y^+}{11}} - y^+\frac{e^{-0.33y^+}}{11}\right) \tag{20}$$

   Here $y^+ = \rho_w u_\tau^* h/\mu_w$ denotes the y-plus value associated with the $h = |\mathbf{x}_{ip} - \mathbf{x}_b|$ distance while ρ_w and μ_w, still denoting the flow density and laminar viscosity at the wall location, respectively, are obtained from field interpolation around the $\mathbf{x}_b$ location.
4. The wall-shear stress first guess, τ_w^*, is then used to estimate the inner-scaled wall spacings, i.e., $\Delta x_w^+ = \Delta x/\delta_\nu$, $\Delta y_w^+ = \Delta y/\delta_\nu$, and $\Delta z_w^+ = \Delta z/\delta_\nu$, being $\delta_\nu = \mu_w/(\rho_w u_\tau^*)$ the viscous length and Δx, Δy and Δz the local grid spacings along the three Cartesian directions, respectively. Thus, according to literature suggestions [4,72], if

$$\Delta x_w^+ < 40, \quad \Delta y_w^+ < 5 \quad \Delta z_w^+ < 20 \tag{21}$$

   the wall portion is considered sufficiently resolved, and the μ_{ip}^{tot} and λ_{ip}^{tot} are directly extrapolated on the ghost point, supposing the laminar behavior of the flow below the image point (wall-resolved hypothesis). The following equations hold:

$$\mu_g^{tot} = 2\mu_w - \mu_{ip}^{tot} \tag{22a}$$

$$\lambda_g^{tot} = 2\lambda_w - \lambda_{ip}^{tot} \tag{22b}$$

5. Conversely, if one of the constraints expressed by Eqs. (21) is not satisfied, the wall model is activated, and a different route of the wall treatment is recovered. A sketch of the method is provided in Fig. 2.

6. In particular, we look at a proper location of the wall-model/LES interface, $\mathbf{x}_{int}$, by searching along the wall-normal direction for the site where the y-plus value reaches a precomputed threshold.
7. Once the $\mathbf{x}_{int}$ is found, flow variables are here interpolated again according to Eq. (15) getting out the interface wall-parallel speed, $u_{//}^{int}$, the interface static pressure, p^{int} and the interface static temperature, T^{int}.
8. Interface flow variables are used as inputs for the solution of Eqs. (10), which in turn give back the wall-modeled velocity, U_{wm}, and temperature T_{wm}, distributions. U_{wm} and T_{wm} are used to calculate the wall-modeled wall shear stress and heat flux according to the following expressions:

$$\tau_w^{wm} = \mu_w \left(\frac{dU_{wm}}{dy} \right)_w \tag{23a}$$

$$q_w^{wm} = \lambda_w \left(\frac{dT_{wm}}{dy} \right)_w \tag{23b}$$

9. Finally, the wall-modeled wall-shear stress and heat flux are enforced as Dirichlet boundary conditions by locally modifying the overall viscosity and diffusivity fields, i.e., by prescribing the so-called effective viscosity and diffusivity at the bound location according to the following expressions:

$$\mu_g^{tot} = 2\mu_{eff} - \mu_{ip}^{tot} \tag{24a}$$

$$\lambda_g^{tot} = 2\lambda_{eff} - \lambda_{ip}^{tot} \tag{24b}$$

Here, μ_{eff} and λ_{eff} denote the effective wall viscosity and diffusivity

$$\mu_{eff} = \frac{\tau_w^{WM}}{\tau_w^{WR}} \mu_w \tag{25a}$$

$$\lambda_{eff} = \frac{q_w^{WM}}{q_w^{WR}} \lambda_w \tag{25b}$$

and precisely denote the missing SGS contribution at the wall required to enforce the correct wall-shear stress and heat flux. Details about the interpretation of μ_{eff} and λ_{eff} are widely provided by De Vanna et al. [45]. Here we claim that this arrangement can effortlessly unify the wall-resolved and the wall-modeled LES approaches, keeping active both the no-slip and no-penetration conditions for the velocity field and the isothermal/adiabatic condition for the temperature at the wall in an arbitrarily shaped bound. Moreover, the effective viscosity and diffusivity values tend to the corresponding laminar values, i.e., $\mu_{eff} \to \mu_w$ and $\lambda_{eff} \to \lambda_w$, while increasing the near-wall resolution progressively.

The overall methodology is described here for 3D z-periodic geometries but can be easily extended to genuinely 3D cases. In particular, Eq. (15) must be reformulated as following:

$$\phi(x, y, z) = \sum_{i,j,k=0}^{1} c_{ijk} x^i y^j z^k \tag{26}$$

being $\{c_i\}$ the interpolation coefficients to be determined. The wall-parallel speed (Eq. (19)), instead, becomes

$$\tilde{u}_{//}^* = \sqrt{(\tilde{u}_{ip} t_1 + \tilde{v}_{ip} t_2 + \tilde{w}_{ip} t_3)^2} \tag{27}$$

The approach is also compatible with potential modifications to a moving-objects framework. In this case, the interpolation coefficients and the geometric contours' position of each submerged object must be determined iteratively. Some hints about possible developments in this path can be recovered from De Vanna et al. [36].

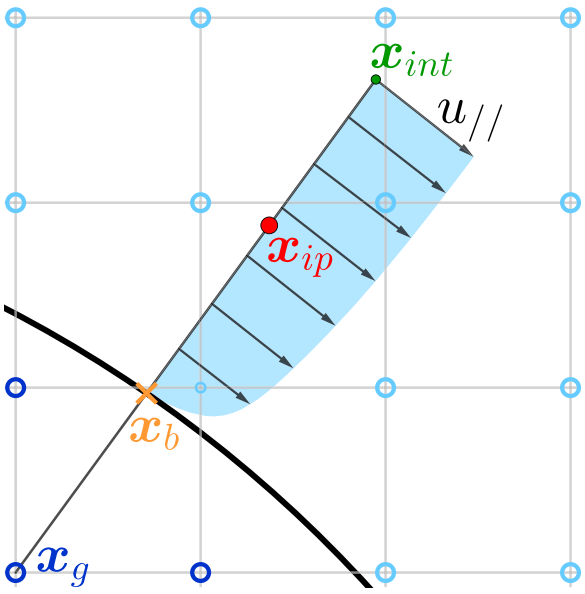

Fig. 2. Sketch of the immersed boundary interpolation procedure.

3.6. Parallelization strategy

A final remark is mandatory about the present methodology. What distinguishes the proposed approach from others in advanced CFD simulations is its easy integrability with multi-GPU logic. The main reason concerns the explicitness of the whole algorithms involved. Compressible Navier–Stokes equations and the suggested immersed boundary approach, in fact, can be handled with entirely explicit schemes, requiring compact supports to deal with all computations. This suits the capacity of contemporary graphics cards, which can perform hundreds of thousands of repetitive and spatially-weakly-linked operations very efficiently. In particular, the core of URANOS has been recently ported to GPU and it is distributed under BSD License 2.0 at the web address https://gitlab.com/fralusa/uranos_gpu [46]. The open-source version of the code collects the whole set of advection/diffusion numerical schemes and turbulence models (DNS, WRLES and WMLES). Thus, URANOS represents an easily extendable platform where CFD developers can test and benchmark their models or applications. The solver's parallelization strategy is based on three different MPI implementations of increasing complexity, from standard SENDRECV blocking routines, through non-blocking ISEND/IRECV calls with sending and receive buffers, up to a non-blocking implementation with MPI-derived datatypes. GPU-enabled computations are made possible with the OpenACC directive-based paradigm in a truly non-vendor-specific framework capable of exploiting contemporary exa-scale computing architectures.

Concerning the immersed solid treatment, and its multi-GPU assessment, geometrical initialization processes are performed with URANOS' external routines. The latter can extract a global array, `imm%b(n)%xlag_gbl`, filling each n-immersed-body-surface boundary points. Bodies' information is then passed to URANOS and handled in an object-oriented fashion to make the process scalable up to an arbitrary number of immersed entities. Consequently, the parallelization strategy in URANOS employs the following steps:

1. The global point array is distributed over processors-based local arrays concerning the proc's bounds, `imm%b(n)%xlag_lcl`.
2. The ray-tracing method by o'Rourke [50] is then used to discern between the solid and fluid domains. In particular, the method examines the global array but flags only the Cartesian points belonging to a local computing unit. This solution allows for

Table 1
Computational settings in the IBM+WMLES channel flow simulations at Mach 0.1.

Case	Marker	$Re_{\tau,0}$	Re_τ	Re_b	$N_x \times N_y \times N_z$	$\Delta x^+ \times \Delta y^+ \times \Delta z^+$
tch1	△	590	596	22162	48 × 78 × 24	77.2 × 7.6 × 77.2
tch2	▷	1000	1010	40265	80 × 78 × 40	78.5 × 16.7 × 78.5
tch3	▽	2000	1982	87530	120 × 104 × 60	104.7 × 25.0 × 104.7
tch4	◁	5200	5376	252442	160 × 156 × 80	204.2 × 43.3 × 204.2
tch5	≺	5200(a)	5118	252442	120 × 104 × 60	272.3 × 65.0 × 272.3
tch6	□	10000	9732	518067	192 × 208 × 96	327.2 × 62.5 × 327.2
tch7	×	10000(a)	9816	518067	120 × 104 × 60	523.6 × 125.0 × 523.6
tch8	◇	20000	19342	1105155	224 × 312 × 112	561.0 × 83.3 × 561.0
tch9	+	20000(a)	19580	1105155	120 × 104 × 60	1047.2 × 250.0 × 1047.2

Table 2
Comparison of fitting coefficients for the $Re_\tau = \alpha Re_b^\beta$ channel flow functional trend.

Case	α	β
Pope law	0.09	0.88
DNS fitting	0.079	0.89
WMLES fitting	0.084	0.89

parallel scalability regarding the number of Cartesian grid points but does not give any speedup due to geometry splitting; however, since the number of points determining the solid surfaces is usually orders of magnitude fewer than the number of Cartesian locations, such a strategy is found to be highly efficient and avoids any compliance with respect to MPI communications inside the ray-tracing kernel.

3. Once the solid location of each computing unit is identified, the Cartesian immersed ghost nodes can be readily determined. An integer marker variable is then used to locally store the information about the various subdomains (i.e., fluid, solid, or solid ghosts).
4. Finally, Cartesian immersed ghost nodes are adopted via local operations to specify the desired boundary condition. The process does not require peculiar MPI treatments since each MPI-rank halo region is sufficiently extended to account for out-of-chank image points and data are already arranged in parallel following the previous steps.

In conclusion, it is important to highlight that these steps are executed only once at the beginning of each simulation. The interpolation coefficients about each ghost node are stored in dedicated buffers defined locally for each processor. A single computational kernel, efficiently distributed over MPI rank or GPU threads, operates over each body's immersed boundary ghost nodes during runtime, efficiently applying the boundary conditions. This approach takes full advantage of GPUs' parallel processing capabilities, enabling a fully parallel algorithm for multi-GPU implementations.

4. Results

The present section discusses the results obtained with the previously described numerical model. In particular, four tests of increasingly complexity are addressed consisting in the channel flow between two immersed block (Section 4.1), a pipe flow inside an immersed block (Section 4.2), a spatially-deploying compressible turbulent boundary layer over a immersed planar surface (Section 4.3), and, finally, a finite-angle-turning turbulent boundary layer over a compression ramp (Section 4.4).

4.1. Channel flow between two immersed blocks

As a first step the turbulent channel flow in a nearly incompressible regime is here presented. The bulk Mach number of the flow, $M_b = u_b/c_w$, is set to 0.1 and a wide range of bulk Reynolds regimes, i.e., $Re_b = 2\rho_b u_b h/\mu_w$, is investigated. Here $u_b = 1/(\rho_b V)\int_V \rho u dV$ is the bulk velocity, $\rho_b = 1/V\int_V \rho dV$ is the bulk density while μ_w and c_w denote the laminar viscosity and the speed of sound at the wall location, respectively. Table 1 reports the bulk Reynolds number of the flow, the nominal, $Re_{\tau,0}$, and the computed, Re_τ, friction Reynolds numbers, being $Re_\tau = h/\delta_\nu$, $\delta_\nu = \mu_w/(\rho_w u_\tau)$ the viscous length, $u_\tau = \sqrt{\tau_w/\rho_w}$ the friction velocity, $\tau_w = \mu_w(\partial u/\partial y)_w$ the wall shear-stress and h the channel half-height. Here it is not worthless to mention that targeting $Re_\tau \approx 2 \cdot 10^4$ is beyond the current computational power if combined with other scale-resolved approaches like DNS or WRLES.

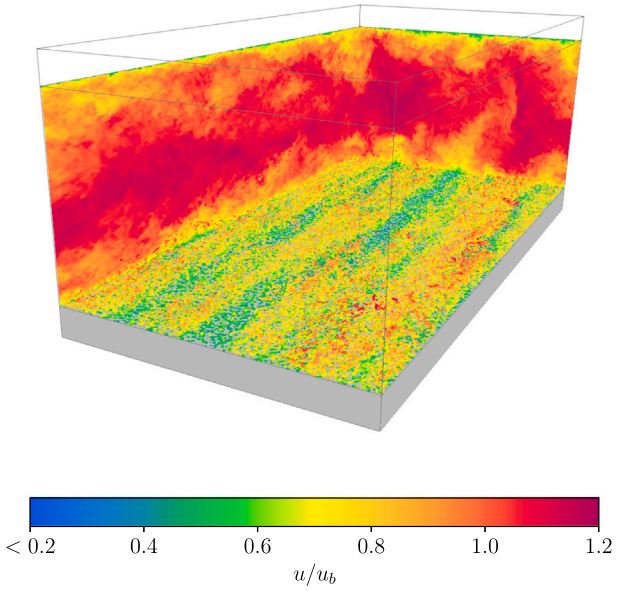

Fig. 3. Instantaneous bulk-scaled velocity contours and Q-criterion for a channel flow confined by two immersed blocks. Present data refer to the $Re_\tau = 10000$ configuration.

Computations are carried out in a tridimensional box with size $L_x \times L_y \times L_z = 2\pi h \times 2.6h \times \pi h$ along the x, y and z coordinates, respectively. In particular, the computational domain is enlarged along with the y direction to include the upper and the bottom IB blocks, acting as immersed walls. These are $0.3h$ each; thus, the flow occupies the inner domain whose height equals $2h$ along with the y direction. A uniform mesh spacing is applied along with all three Cartesian coordinates. The number of nodes, $N_x \times N_y \times N_z$, and the corresponding mesh spacings in inner units (i.e., normalized by the viscous length, δ_ν), $\Delta x^+ \times \Delta y^+ \times \Delta z^+$, are reported in Table 1. It is worth noting that Table 1 reports the results of $Re_\tau = \{5200, 10000, 20000\}^T$ configurations using two different resolutions. The first entails a linear increase in the spatial resolution, and the second, (a)-cases, keeps the same resolution as in the $Re_\tau = 2000$ setup.

Regarding boundary conditions, periodicity is enforced in the wall-parallel directions, while the two immersed walls are subject to a no-slip isothermal condition with shear stress and heat flux imposed according to the IBM+WMLES procedure. The initial condition is obtained according to the method of Henningson and Kim [79], which

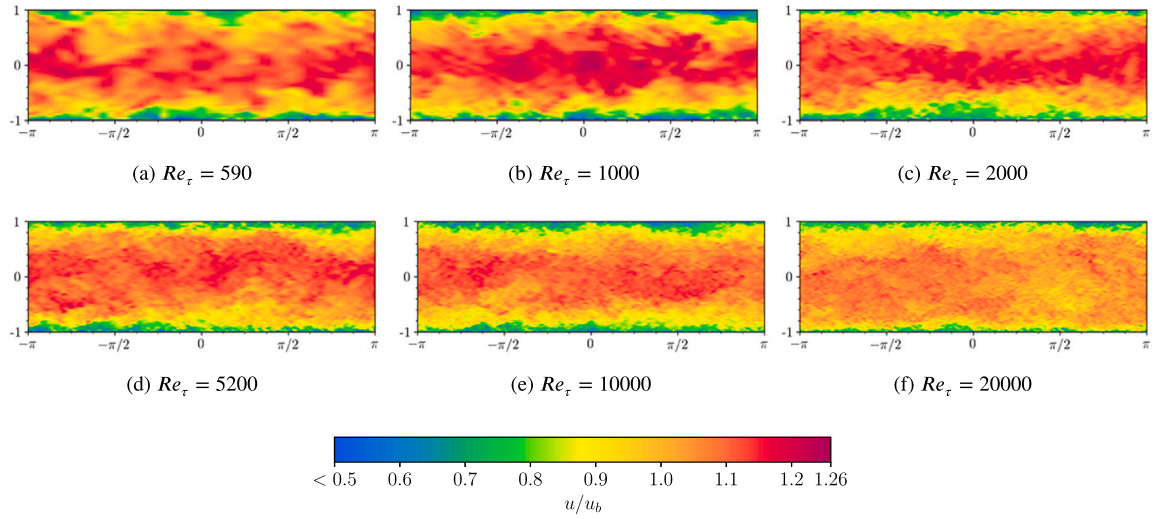

Fig. 4. Channel flow bulk-scaled instantaneous velocity contours as a function of the friction Reynolds number.

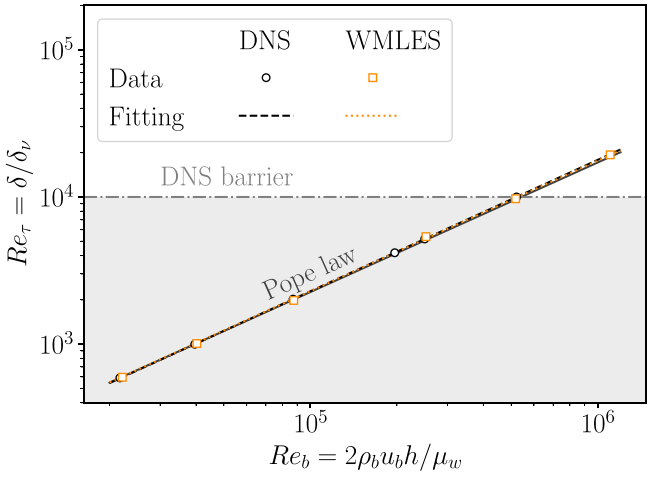

Fig. 5. Friction Reynolds number trend as a function of the bulk Reynolds number for channel flow configurations. Present IBM+WMLES computations are compared to available DNS results [73–77] as well as suggestions provided by Pope [78].

superimposes a vortex pair over the analytical solution of the Poiseuille flow. Such a strategy encourages a rapid transition to turbulence without exceeding complex initial states. To keep the flow rate in the channel constant, a forcing term $f_i = \{0, f, 0, 0, fu\}^T$ is added to the Navier–Stokes right-hand-side. At each time step, the latter is assessed; thus, discretely ensuring mass flow rate conservation. Since the flow is shock-free, convective terms are discretized with the sixth-order EP scheme in a pure state.

Fig. 3 shows the instantaneous bulk-scaled velocity field, u/u_b, concerning the $Re_\tau = 10^4$ configuration. To this, the iso-surfaces associated with the Q-criterion for vortex visualization is over-imposed. For clarity, the upper IB block is just sketched, and only the lower bound is reported. From such a qualitative representation, we can observe how the system dynamics are characterized by fully developed turbulence. In particular, the system's large scales of motion are clearly evident and alternate between slow and fast streaks. Thus, from first sight, the method seems able to grasp the complex dynamics associated with a wall flow at such high Reynolds conditions. Fig. 4, instead, displays the instantaneous bulk-scaled velocity fields as a function of the Reynolds regimes, i.e., moving from $Re_\tau = 590$ up to 20000.

Moving on to more quantitative results, the friction Reynolds number trend is investigated as a function of the bulk Reynolds numbers of the flow. According to Pope [78], the $Re_\tau = f(Re_b)$ functional trend is well fit by the following expression:

$$Re_\tau = \alpha Re_b^\beta \tag{28}$$

where α and β are fitting constants. Pope suggests $\alpha = 0.09$ and $\beta = 0.88$, respectively. Fig. 5 reports the $Re_\tau = f(Re_b)$ trend according to Ref. [78] and compares available DNS data to present WMLES computations. Obtained results are well aligned with both DNS computations and trend predictions, even out of the DNS range, whose upper bound is highlighted by a dash-dotted gray line. Table 2 reports α and β coefficients comparison as a function of the adopted methodologies. As the reader can observe, the present IBM+WMLES method perfectly fits both theoretical and DNS fitted values.

Finally, Fig. 6 reports single point statistics. In particular, Figs. 6(a) and 6(b) show the inner-scaled velocity profiles, $\tilde{u}^+ = \tilde{u}/u_\tau$, and the inner-scaled turbulent kinetic energy, $\tilde{k}^+ = \widetilde{u_i'' u_i''}/u_\tau^2$, respectively, as a function of the inner-scaled wall distance, $y^+ = y/\delta_\nu$. For greater clarity, velocity distributions are offset in the vertical direction by five wall unit steps. Apart from some mild log-layer mismatch, typical of WMLES computations, overall, the results are well aligned with DNS references by Vreman and Kuerten [73], Bernardini et al. [74], Lee and Moser [75], Hoyas et al. [76], Oberlack et al. [77] for both mean quantities and fluctuations. Furthermore, it is worth noting that configurations with $Re_\tau > 2000$ exhibit minimal sensitivity to the chosen resolution. In such cases, the model accurately represents both the mean velocity profile and the fluctuations, achieving a level of accuracy similar to configurations with higher resolutions. This behavior arises due to the model's capability to effectively predict wall dynamics once scale separation is achieved, i.e., as long as the outer layer is resolved. Consequently, given the constant boundary layer height of h in a channel flow, the model exhibits near insensitivity to the Reynolds number. Finally, data are also provided for a nominal Re_τ of $2 \cdot 10^4$. The latter are compared with Reichardt's law [71] since no DNS or experiments are available for such a Reynolds regime. The trend is confirmed even for such extreme configurations.

4.2. Turbulent pipe flow inside an immersed block

As the next step, the proposed procedure is tested in a non-conformal geometrical arrangement; thus, a turbulent pipe flow embedded inside an immersed block is addressed. The setup is similar to that of the channel flow. Such a geometric arrangement has been selected precisely in light of stressing the method to deal with arbitrary cut cells since the position of the first-off-the-wall grid point concerning the immersed

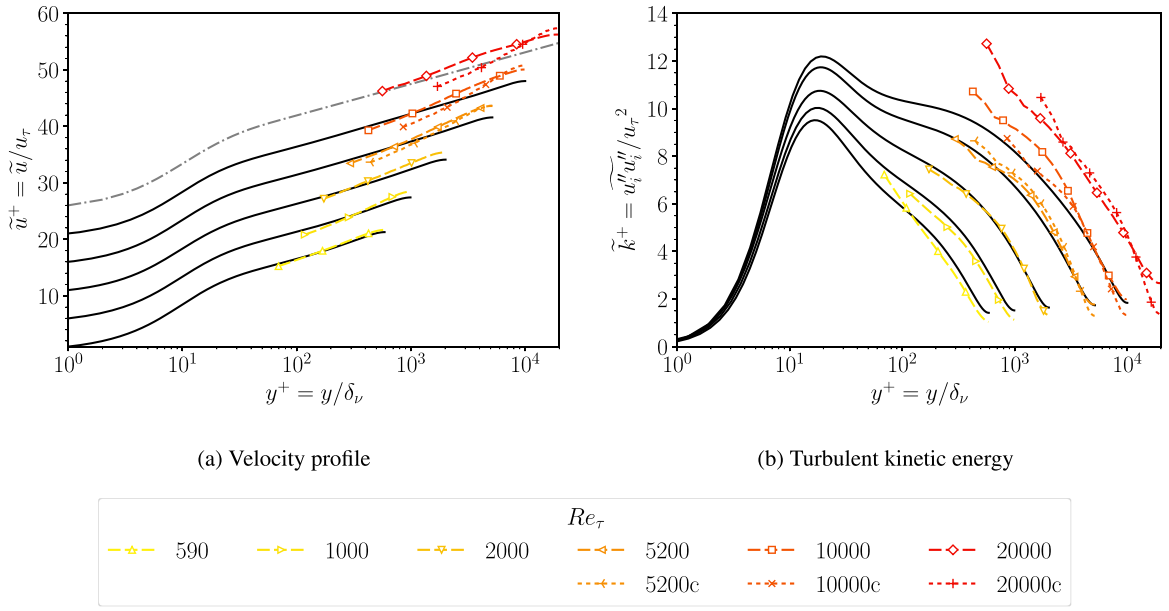

(a) Velocity profile

(b) Turbulent kinetic energy

Fig. 6. Inner-scaled velocity distributions, $u^+ = \tilde{u}/u_\tau$, and inner-scaled turbulent kinetic energy, $\tilde{k}^+ = \widetilde{u_i'' u_i''}/u_\tau^2$, as a function of the inner-scaled wall distance, $y^+ = y/\delta_\nu$, for channel flow setups at $M_b = 0.1$ and Re_τ up to $2 \cdot 10^4$. Present results (colors with dots) are compared with DNS data (solid black lines) by Vreman and Kuerten [73],Bernardini et al. [74],Lee and Moser [75],Hoyas et al. [76],Oberlack et al. [77] and with analytical reference according to the Reichardt's law [71].

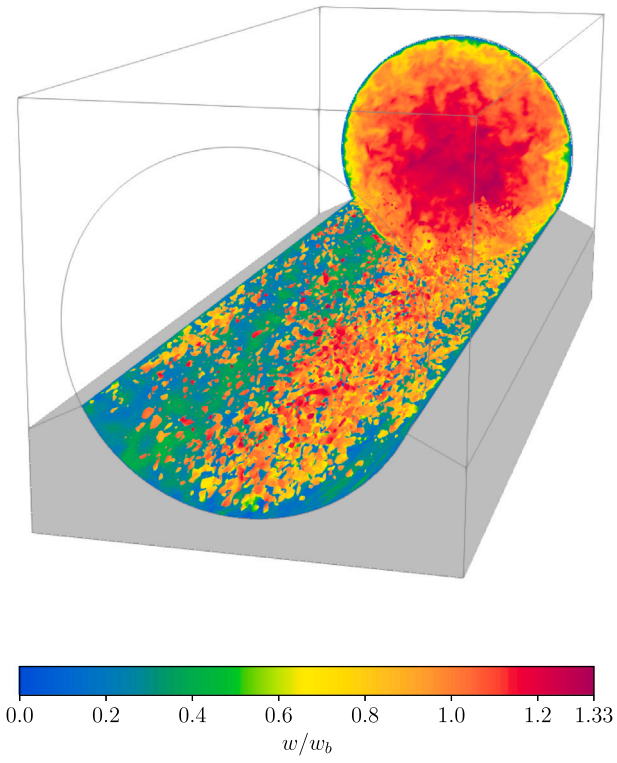

Fig. 7. Instantaneous bulk-scaled velocity contours and Q-criterion for a pipe flow confined inside an immersed block. Present data refer to the $Re_\tau = 6000$ configuration.

contour is not directly controllable. The flow's bulk Mach number, $M_b = w_b/c_w$, is still set to 0.1, and a wide range of bulk Reynolds numbers, $Re_b = 2\rho_b w_b R/\mu_w$, is investigated. Here R denotes the pipe radius while the z axis is selected as the streamwise coordinate, so that bulk speed is denoted by $w_b = 1/(\rho_b V)\int_V \rho w dV$.

The computational domain is made up of a rectangular box of size $2.4R \times 2.4R \times 2\pi R$ and is discretized with a uniform Cartesian grid in all directions according to the description reported in Table 3. With this arrangement, the flow occupies a cylindrical sector of radius R, while the rest of the domain is reserved for the IB block. Table 3 reports the nominal ($Re_{\tau,0}$) and the computed (Re_τ) friction Reynolds number of the flow, being $Re_\tau = R/\delta_\nu$, together with the bulk Reynolds number, Re_b. Mesh characteristics are also provided in term of the number of computing nodes, $N_x \times N_y \times N_z$, and mesh spacings in inner units, $\Delta\theta^+ \times \Delta r^+ \times \Delta z^+$, being θ, r and z the azimuthal, the radial and the axial coordinate directions, respectively. Conversely to the channel flow, δ_ν, the viscous length, is defined as $\delta_\nu = \mu_w/(\rho_w w_\tau)$ being $w_\tau = \sqrt{\tau_w/\rho_w}$ the friction velocity and $\tau_w = \mu_w(\partial w/\partial y)_w$ denoting the wall shear stress, with $y = R - r$ the wall normal coordinate.

Concerning the boundary conditions, the external IB block is modeled as a no-slip and isothermal wall that enforces proper wall shear stress and heat flux values according to the IBM+WMLES procedure. Periodicity is enforced along with the pipe axial direction, while no peculiar boundaries are associated with the edge of the computational domain since they do not affect the flow. Again the procedure proposed by Henningson and Kim [79] is used to initialize the system mechanics. In particular, a vortex pair is over-imposed on the analytical solution of the Poiseuille flow in radial coordinates. The mass-flow rate is discretely enforced by adding $f_i = \{0, 0, 0, f, fu\}^T$ as an external force to the Navier–Stokes right-hand side. Again, since no shocks/shocklets afflict the flow, the sixth-order EP scheme in a pure state is used for convective terms discretization.

Fig. 7 displays a qualitative overview of the computational domain and the flow. The bulk-scaled velocity field and the Q-criterion for vortex visualization are reported. As shown, the fluid domain is surrounded by a square section block made up of the domain's IB border. For clarity, the latter is only partially displayed.

As in the channel flow case, Fig. 8 displays the influence of the Reynolds number in the pipe dynamics from a strictly qualitative perspective. Here, x–y plane cuts related to the four investigated configurations, ranging from $Re_\tau = 500$ up to 6000, are provided. The reader can observe that the overall turbulence pattern is enriched with ever finer coherent structures as the grid density increases. Despite this, the core of the flow, essentially homogeneous and isotropic, is well represented by the primary eddy-viscosity turbulence model and gathered realistically.

Table 3
Computational settings in the IBM+WMLES pipe flow simulations at Mach 0.1.

Case	Marker	$Re_{\tau,0}$	Re_τ	Re_b	$N_x \times N_y \times N_z$	$\Delta\theta^+ \times \Delta r^+ \times \Delta z^+$
tpi1	△	500	551	18433	96 × 96 × 50	13.8 × 13.8 × 69.2
tpi2	▷	1140	1217	46862	128 × 128 × 96	22.7 × 22.7 × 79.2
tpi3	▽	3000	3183	138105	128 × 128 × 96	59.7 × 59.7 × 208.3
tpi4	◁	6000	6398	297070	150 × 150 × 96	102.4 × 102.4 × 418.8

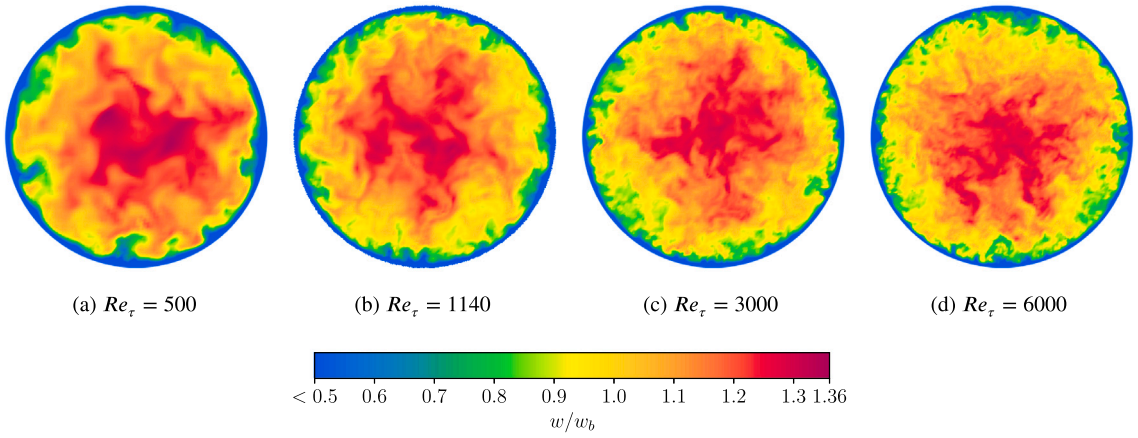

Fig. 8. Pipe flow bulk-scaled instantaneous velocity contours as a function of the friction Reynolds number.

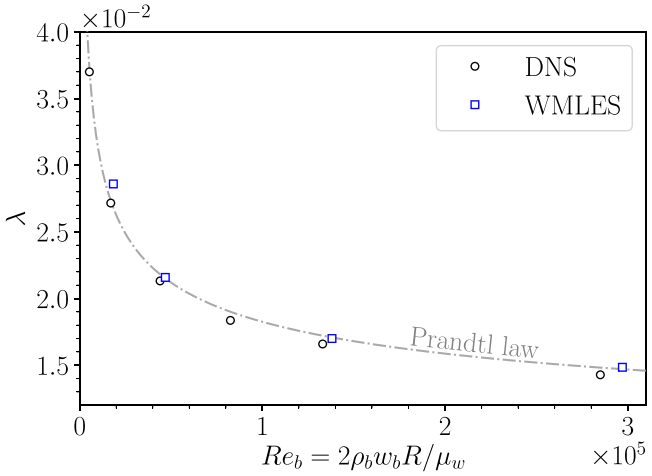

Fig. 9. Friction factor as a function of bulk Reynolds number for pipe flow configurations. Present IBM+WMLES computations are compared to DNS by Pirozzoli et al. [80]. The dashed-dotted line denotes the Prandtl fitting law.

Looking at more quantitative aspects, Fig. 9 reports the pipe friction factor, λ, as a function of the bulk Reynolds number of the flow, being λ defined as:

$$\lambda = \frac{8\tau_w}{\rho_b w_b^2} \tag{29}$$

A precise forecast of such a parameter enables us to conclude that the system has established the proper dynamic equilibrium condition in which wall friction and mass flow rate are entirely consistent. On a technical level, the friction factor for a smooth pipe is often calculated using the Prandtl law, which states:

$$\frac{1}{\lambda^{1/2}} = A \log_{10}(Re_b \lambda^{1/2}) - B \tag{30}$$

Here $A = 2.0$ and $B = 0.8$ are fitting parameters derived from Nikuradse [81] experiments. Thus, Fig. 9 compares the friction factor values obtained with the current IBM+WMLES approach to the Pirozzoli et al. [80] DNS data. The dashed gray line reports the Prandtl law trend. As seen, findings are almost superimposed to both DNS and Prandtl fitting, with a mild exception for the lowest Reynolds configuration that is slightly overestimated. The rationale for this has to be found in the wall model's assumptions, which imply a fully developed turbulent flow and a thin boundary layer hypothesis. Indeed, when the Reynolds number increases, the WMLES perfectly recovers the DNS datum and Prandtl law.

Finally, Fig. 10 reports single point statistics comparison with DNS data. In particular, the ensemble-averaged inner-scaled velocity profiles, $w^+ = \tilde{w}/w_\tau$, (Fig. 10(a)) and the ensemble-averaged inner-scaled turbulent kinetic energy, $\tilde{k}^+ = \widetilde{u_i'' u_i''}/u_\tau^2$ (Fig. 10(b)) are provided as a function of the inner-scaled wall distance, $y^+ = y/\delta_\nu$. For greater clarity, velocity profiles are still offset in the vertical direction by five wall unit steps. As the reader can notice, results well agree with the DNS references by Pirozzoli et al. [80]. In particular, mean velocity distributions perfectly overlap the DNS solution, while mild deviation in velocity fluctuations are observed with the model systematically underestimating the reference. Such results, considered the adopted resolutions, allows us to confirm the quality of the methodology applied to a non-conformal geometry in high-Reynolds number regimes.

4.3. Compressible turbulent boundary layer over an immersed block

As a further step we present results obtained by simulating a turbulent boundary layer in a compressible regime. The simulation is modified compared to canonical setups and, in particular, the boundary layer evolution is made to spatially-deploying over an immersed block. We consider four $M_\infty = u_\infty/c_\infty = 2$ configurations with adiabatic wall conditions targeting the location along the plates where $Re_{\tau,0} = \delta/\delta_\nu$ is equal to 250, 580, 1110 and 2000. The first three Reynolds regimes are selected since we dispose of DNS references by Pirozzoli and Bernardini [57], while the last configuration aims at proving the predictive capability of the model in high-Reynolds conditions. Fixing the mathematical notation, here u_∞ and $c_\infty = \sqrt{\gamma R T_\infty}$ are the free-stream velocity and speed of sound, respectively; δ denotes the 99% freestream-speed-recovery local boundary layer thickness; $\delta_\nu = \mu_w/(\rho_w u_\tau)$ is the local viscous length; μ_w, ρ_w and u_τ still denote the laminar wall viscosity, the fluid wall density, and the wall friction velocity, respectively.

All simulations are carried out in a three-dimensional box of size $L_x \times L_y \times L_z = (90 \times 11 \times 6)\delta_0$, being δ_0 the nominal inflowing boundary

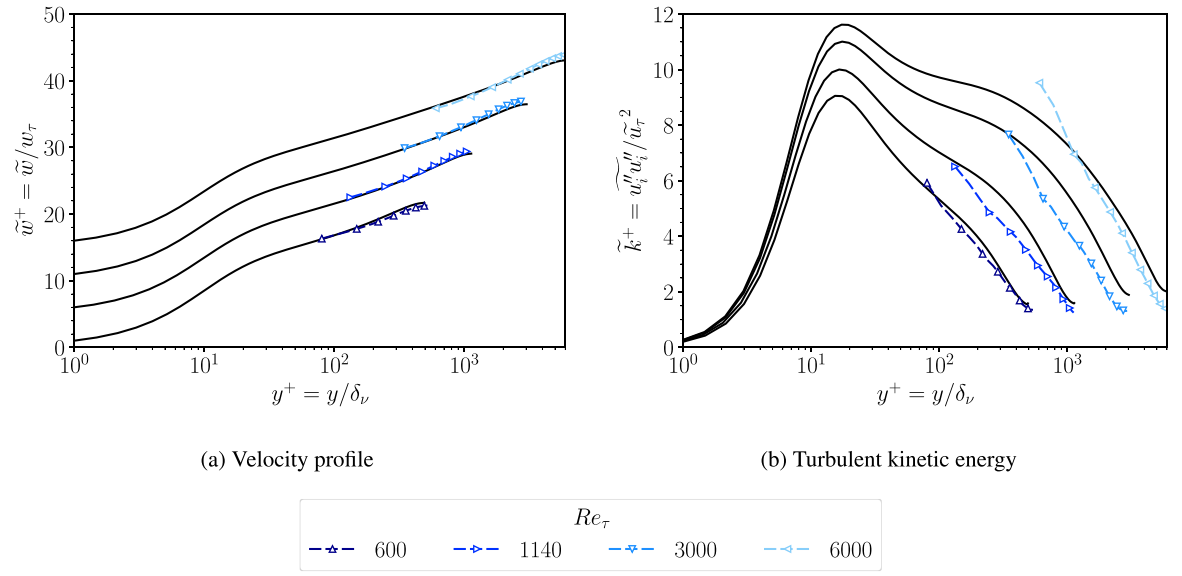

(a) Velocity profile (b) Turbulent kinetic energy

Fig. 10. Mean streamwise velocity profiles, $w^+ = \tilde{w}/w_\tau$, and inner-scaled turbulent kinetic energy, $\tilde{k}^+ = \widetilde{u_i'' u_i''}/u_\tau^2$, as a function of the inner-scaled wall distance, $y^+ = y/\delta_\nu$, for pipe flow cases at $M_b = 0.1$ and Re_τ up to 6000. Present results (colors with dots) are compared with DNS data (solid black lines) by Pirozzoli et al. [80].

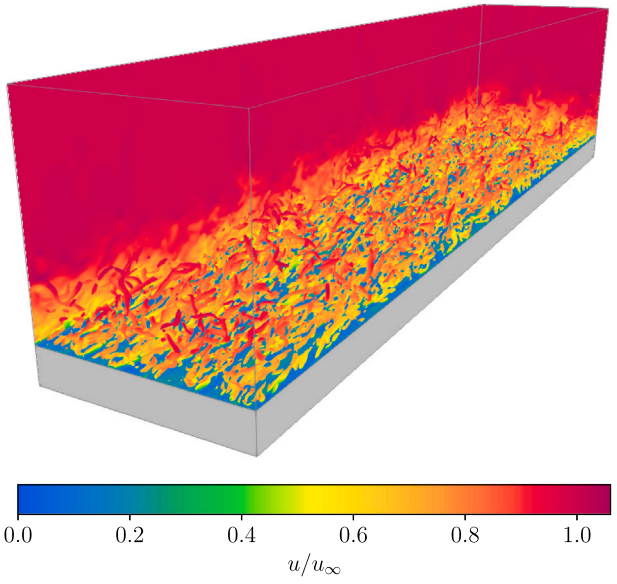

Fig. 11. Instantaneous freestream-scaled velocity contours and Q-criterion for a turbulent boundary layer confined by one immersed block. Present data refer to the $Re_\tau = 1110$ configuration.

layer thickness. In particular, as in the channel flow, the computational domain is enlarged along with the wall-normal direction. Thus, a length equal to $10\delta_0$ is reserved for the flow motion while a space of δ_0 is reserved to accommodate the immersed block. The streamwise direction, instead, is made long enough to capture the large-scale and intermittent motions associated with turbulent structures and avoid possible statistical correlation with the inflowing synthetic turbulence generation. Along with all three Cartesian directions, uniform grids are adopted.

Table 4 summarizes the simulation parameters. Here, the marker style, the target ($Re_{\tau,0}$) and the computed friction Reynolds numbers (Re_τ), the number of points, $N_x \times N_y \times N_z$, and the mesh spacing in viscous units, $\Delta x^+ \times \Delta y^+ \times \Delta z^+$, are reported.

Regarding boundary conditions, fully three-dimensional Navier–Stokes Characteristic Boundary Conditions (NSCBCs) [82,83] are imposed at the top and right bounds of the domain. Thus, characteristic decomposition and the evolution of transverse and viscous terms are adopted. The approach delivers the correct outflow behavior with minimum acoustic wave reflection or spurious oscillation injection. At the bottom wall, an IB block is used as a no-slip and non-penetrating condition combined with the wall-modeling strategy. In particular, according to the present wall-modeled LES process, the IB block enforces all velocity components to zero, the wall temperature isothermality, the correct friction, and wall heat-flux. The isothermal condition is imposed by prescribing

$$\frac{T_w}{T_\infty} = T_{rat}\left[1 + \frac{r}{2}(\gamma - 1)M_\infty^2\right] \tag{31}$$

Here T_w/T_∞ is the freestream-scaled wall temperature, $r = Pr^{1/3}$ denotes the recovery factor, while $T_{rat} = T_r/T_{ad}$ is the ratio between the recovery temperature and the nominal adiabatic temperature. In present computations, T_{rat} is set to one; thus, the wall behaves as purely adiabatic. As customary in LES, the spanwise flow is considered to be statistically homogeneous, and periodic boundaries are used. The inflow condition is implemented following the synthetic digital filter approach by Klein et al. [84]. In particular, the improved version by Kempf et al. [85] is used. Thus, velocity fluctuations are overlaid with Musker's nominal turbulent mean velocity profile [86]. The process grants a quick transition to a fully developed turbulent boundary layer that reaches stability around $10\delta_0$ downstream of the inflow location. Finally, concerning numerical methods, the present calculation is performed with a hybrid EP-TENO-A 7 convective scheme, setting Ducros level to $\bar{\theta} = 0.1$. Such a numerical arrangement increases the simulation's stability without excessively penalizing the natural deployment of the wall turbulence [68].

Fig. 11 shows the instantaneous freestream-scaled velocity field, u/u_∞, for the $Re_\tau = 1110$ arrangement. Specifically, the Q-criterion for vortices visualization is over-imposed on the wall-normal streamwise parallel instantaneous velocity contours. Color shades are linked to the speeds range. Thus, lower velocities are associated with blue tones, while peaks are reported with dark red. In the bottom section of the domain, the immersed boundary block, acting as the wall-modeled LES condition, is reported. The reader may appreciate the high amount of

Table 4
Computational settings in the IBM+WMLES compressible turbulent boundary layer flow simulations at Mach 2.0.

Case	Marker	$Re_{\tau,0}$	Re_τ	$N_x \times N_y \times N_z$	$\Delta x^+ \times \Delta y^+ \times \Delta z^+$
tbl1	△	250	252	256 × 78 × 48	87.9 × 17.6 × 31.3
tbl2	▷	580	586	600 × 156 × 96	87.0 × 20.4 × 36.3
tbl3	▽	1110	1127	1200 × 224 × 192	83.3 × 27.3 × 34.6
tbl4	◁	2000	2013	1500 × 280 × 240	120.0 × 39.3 × 50.0

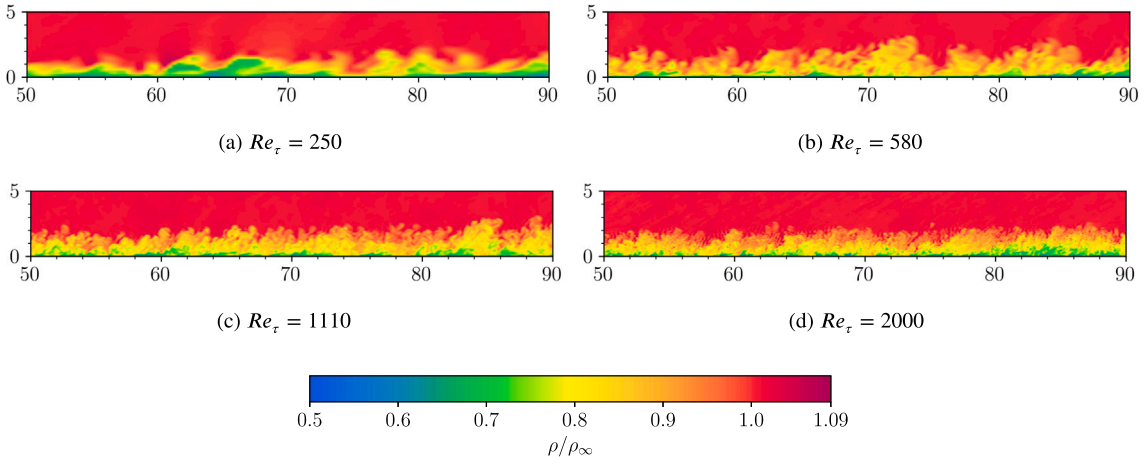

Fig. 12. Boundary layer freestream-scaled instantaneous density contours as a function of the friction Reynolds number.

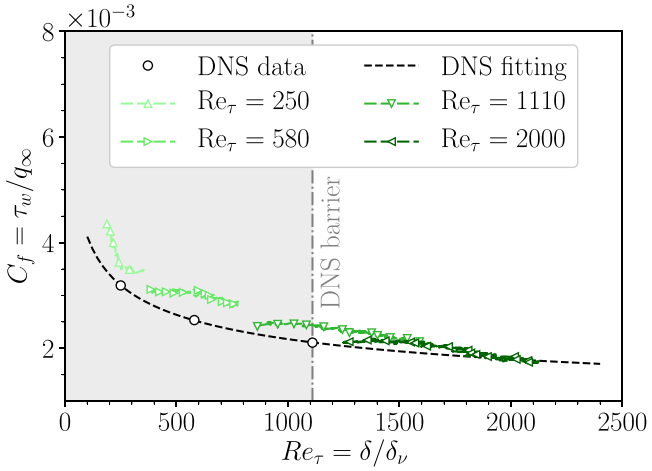

Fig. 13. Friction coefficient as a function of the friction Reynolds number for a boundary layer over a flat plate a Mach 2. DNS trend fits $C_f = aRe_\tau^b$.

turbulence in the flow and the model's ability to properly represent more prominent turbulent structures.

Fig. 12 depicts the instantaneous freestream-scaled density fields over wall-normal slices. Data are provided parametrically with the friction Reynolds number. Similarly to previous color maps, results display rarefied regions with blue shades, while higher-density areas are reported with yellow and red tones. From these purely qualitative representations, we immediately recognize the role of the Reynolds number concerning turbulence deployment. In particular, as the Reynolds regime increases, turbulent structures become finer and finer, making the model able to grasp the system's physics very well, at least from a qualitative point of view.

Moving on to quantitative results, Fig. 13 shows the friction coefficient trend, $C_f = \tau_w/q_\infty$, as a function of the local friction Reynolds number, Re_τ. In particular, DNS data by Pirozzoli and Bernardini [57] are compared to present IBM+WMLES computations. It should be emphasized that the highest DNS Reynolds regime attains to $Re_\tau = 1110$; therefore, the proposed model is used in a predictive way to analyze a wall flow at a Reynolds number double the maximum available in the literature. Not having data for comparison at $Re_\tau = 2000$, DNS results are fitted and extrapolated beyond their range, assuming a polynomial trend for the friction coefficient. In particular, the following functional behavior is assumed:

$$C_f = aRe_\tau^b \tag{32}$$

which describes a standard behavior of the friction coefficient in boundary layer flow over a flat plate [78,87]. Regression process gives $a = 0.01474596$ and $b = -0.27720095$. Fig. 13 demonstrates how the data collected with the proposed model well match the DNS trend. In particular, we see that the model always tends to slightly overestimate the DNS value, even though the overestimation steadily diminishes as the Reynolds number grows. This is readily explicable given that the wall model assumes a fully developed turbulent flow with large-scale separations in the boundary layer. Thus, the fact that findings suit the DNS trend better and better as Re_τ grows is consistent with the model hypothesis.

Finally, moving to wall-normal statistics, Fig. 14 shows the mean streamwise inner-scaled velocity profile, $u^+ = \tilde{u}/u_\tau$, and the inner-scaled turbulent kinetic energy, $\tilde{k}^+ = \bar{\rho}\widetilde{u_i''u_i''}/\tau_w$, as a function of the inner-scaled wall distance, $y^+ = y/\delta_\nu$. Very good agreement is recovered where DNS are disposed, while the $Re_\tau = 2000$ setup simply confirms the trend.

4.4. Finite-angle-turning supersonic boundary layer over a compression ramp

As a conclusive assessment to characterize the proposed numerical strategy, the present section outlines the interaction between a $\theta = 24°$ compression ramp and turbulent boundary layer in highly-compressible conditions. Simulations faithfully replicate the DNS setup described by Priebe and Martín [88]. In particular, freestream conditions suppose a $M_\infty = u_\infty/c_\infty = 2.91$ flow. Thus, the arrangement induces an oblique shock wave sticking to the ramp leading edge with a nominal inviscid angle of $\beta = 43.58°$. The DNS database supposes the inflowing boundary layer with a nominal friction Reynolds number, $Re_\tau = \delta/\delta_\nu$,

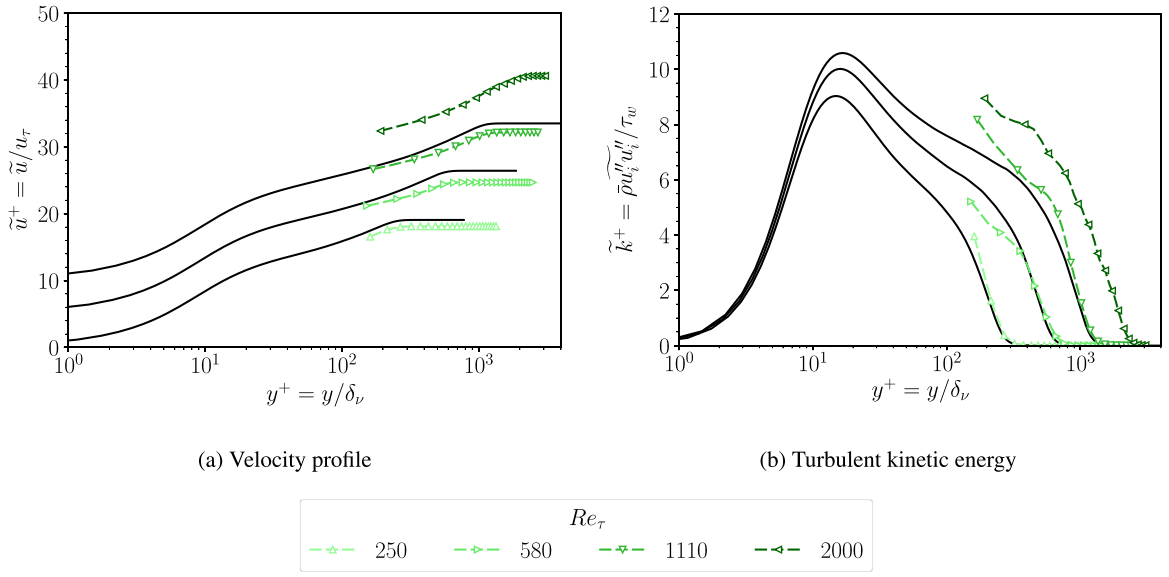

(a) Velocity profile (b) Turbulent kinetic energy

Fig. 14. Mean streamwise velocity profiles, $u^+ = \tilde{u}/u_\tau$, and inner-scaled turbulent kinetic energy, $\tilde{k}^+ = \widetilde{\rho u_i'' u_i''}/\tau_w$, as a function of the inner scaled wall distance, $y^+ = y/\delta_\nu$, for boundary layer cases $M_\infty = 2.0$ and Re_τ up to 2000. Present results (colors with dots) are compared with DNS data by Pirozzoli and Bernardini [57].

of around 320 at the shock foot. The complex interaction between the turbulent boundary layer and the shock wave, together with the adverse pressure gradient, causes flow separation in the ramp's leading edge area. For the present test, the mathematical notation recovers the same convections adopted in Section 4.3. Thus, u_∞ and c_∞ still represent the freestream velocity and speed of sound, respectively; δ is the 99% boundary layer thickness; $\delta_\nu = \mu_w/(\rho_w u_\tau)$ denotes the local viscous length, while μ_w and ρ_w are the laminar wall viscosity and flow density at the wall location, respectively. Simulations are carried out in a three-dimensional box of size $L_x \times L_y \times L_z = 80\delta_0 \times 21\delta_0 \times 10\delta_0$, being δ_0 the nominal inflowing boundary layer thickness. Again, the domain is enlarged by one unit delta along with the y-direction to accommodate the immersed body. The last for the geometrical setup is the ramp leading edge location which is placed $50\delta_0$ downstream of the inflow edge to avoid any statistical correlation with the synthetic turbulence generation.

The boundary conditions receipt adopted for the spatial deploying turbulent boundary layer is replicated here. Thus, NSCBCs are enforced at the top and the right domain edges, while the solid surface is treated as a single IB block. The latter drives all velocity components to zero, assures the desired wall temperature, and enforces the correct wall shear stress and heat flux according to the proposed IBM+WMLES procedure. Wall temperature is still prescribed according to Eq. (31), where T_{rat}, the ratio between the recovery and the adiabatic nominal temperatures, is set to 0.87; the value fitting the DNS prescriptions by Priebe and Martín [88]. Periodic boundary conditions are enforced along with the spanwise direction, while inflow turbulence is provided again with the enhanced synthetic digital filter approach by Klein et al. [84] and Kempf et al. [85]. Finally, calculations are performed with a hybrid EP-TENO-A 5 convective scheme with a Ducros threshold, $\bar{\theta}$, equal to 0.1.

4.4.1. Spatial resolution

Present IBM+WMLES computations are performed over three increasingly refined meshes, the details of which are reported in Table 5. The meshing approach, in particular, includes the non-uniformly spreading of computational nodes in the x–y plane to focus the computational effort on the solution of the incoming boundary layer and the ramp section. The spanwise direction, instead, is discretized with constant spacing. Because the ramp turning angle is intense, the grid clustering process results in an over-resolution for the incoming boundary layer. In fact, if the portion of the flat plate had not been over-resolved concerning the usual WMLES canons, the de-refinement process would have produced an excessive under-resolution for the sloped section, making it difficult to resolve the ramp even from a geometrical standpoint. Table 5, in particular, reports the marker style, the target ($Re_{\tau,0}$) and the computed (Re_τ) Reynolds numbers at the shock foot location, as well as the extension of the separation bubble, giving the non-dimensional separation $x^*_{sep} = (x_{sep} - x_{le})/\delta$, and the reattachment, $x^*_{rea} = (x_{rea} - x_{le})/\delta$, locations. Here x_{le} denotes the ramp leading edge location. Due to the complex nature of the flow, spatial resolutions are graphically provided. Thus, mesh spacing distributions along with the body surface are provided in Fig. 15. In particular, Figs. 15(a)–15(c) report, respectively, the ensemble-averaged Δx^+_w, Δy^+_w and Δz^+_w distributions along with the solid surface as a function of the non-dimensional streamwise coordinate, $x^* = (x - x_{le})/\delta$, and parametrically to the adopted mesh. WRLES thresholds, according to Eq. (21), are also reported as nominal references. Here it is worth noting that grid-scaled units, $\Delta x^+_{w,i} = \Delta x_{w,i}/\delta_\nu$, are not well-posed for the out-of-equilibrium flows since the viscous length, δ_ν, vanishes at the boundary layer separation/reattachment locations. However, since the wall model is instantaneously activated/deactivated based on $\Delta x^+_{w,i}$ local values, the post-processed grid-scaled units are accumulated as a single term, so that by averaging $\Delta x^+_{w,i} = \Delta\widetilde{x_{i,w}}/\delta_\nu$. For this reason, the resulting grid-scaled units reflect exactly the ensemble-averaged activation/deactivation of the model based on the local quantities.

Table 5
Computational settings in the IBM+WMLES Mach 2.91 turbulent boundary layer over a compression ramp.

Case	Marker	$Re_{\tau,0}$	Re_τ	x^*_{sep}	x^*_{rea}	$N_x \times N_y \times N_z$
Coarse	▽	320	315	−4.0	0.56	768 × 384 × 80
Medium	◁	320	320	−4.0	0.80	1024 × 512 × 96
Fine	△	320	340	−3.2	0.67	1536 × 768 × 128

4.4.2. Instantaneous flow description

Going to describe the overall system dynamics, Fig. 16 qualitatively shows the three-dimensional flow deployment. Here, the Q-criterion for vortices visualization is superimposed on the instantaneous Schlieren density contour reported in the backplane. The color map provides the Mach number local value. From such a qualitative representation, three most significant parts can be immediately recognized:

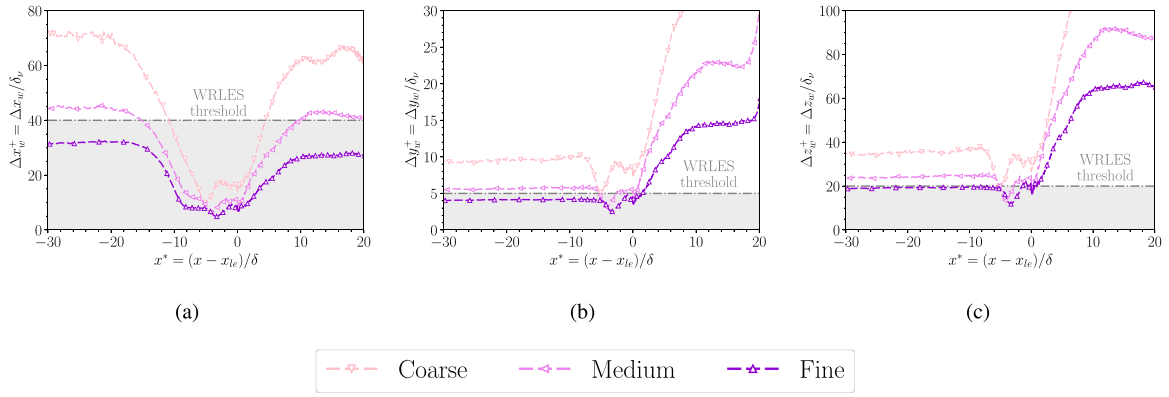

Fig. 15. Near-wall resolutions in internal spacing as a function of the streamwise coordinate.

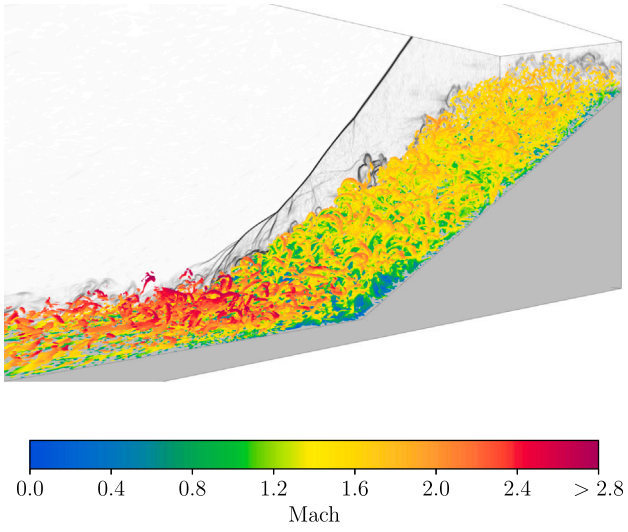

Fig. 16. Instantaneous Schlieren density and Q-criterion contours for a supersonic ramp. Present data refer to Medium mesh.

1. The first portion (yellow to red tones) embeds the incoming boundary layer on top of the initial flat plate. The flow is here characterized by a near-to-nominal average Mach number, and the boundary layer is entirely in equilibrium with the wall.
2. The second flow section (blue to green tones) follows the incoming boundary layer region, and it is mainly characterized by the recirculation region. Here, the boundary layer interacts with the shock wave, which is plainly visible on the background plane's Schlieren trace. Around the ramp leading edge, the flow tends to stagnate due to the negative pressure gradient, resulting in a recirculation bubble.
3. Finally, the third part (green to yellow shades) consists in the recovering boundary layer over the sloped surface where the flow recovers the stability and keep on going through the outlet.

A more extensive examination of the flow's instantaneous development is reported in Fig. 17. Here a zoom of the instantaneous freestream-scaled x-velocity component near the ramp leading edge is reported for a $x - y$ slice of the domain. Color maps show the velocity range from blue to red tones and offer findings for the three increasingly refined meshes used in the present computations. Velocity slices confirm the qualitative description of the flow we discussed by looking at the three-dimensional field deployment. However, the recirculation zone and the non-stationary shock wave trace are enhanced here, with the noteworthy aspect of detecting negative velocity values. This aspect is peculiar since the wall model, supposing the equilibrium of the boundary layer, theoretically rules out adverse velocity gradient events. This fact is, therefore, to be framed in the WR/WMLES blending process, which allows for treating sufficiently-resolved flow zones through a wall-resolved approach. Coming back to Figs. 15, the grid-scaled units in the recirculation area allow the model to act by a large margin as a wall-resolved approach.

In this path it is interesting to look at the activation and deactivation of the wall model over the ramp surface quantitatively as a function of the grid resolution. We said that if Eq. (21) is met locally, the current IBM+WMLES strategy automatically shifts to a WRLES-type approach. This is obtained according to a side algorithm embedded in the wall-modeling procedure that, in such occurrences, avoids introducing any additional artificial viscosity/diffusivity. Fig. 19 describes the activation of the wall model quantitatively by reporting the ensemble-averaged WMLES activation sensor trend, θ_{WM}, as a function of the non-dimensional streamwise coordinate and parametrically to the mesh refinement level. The sensor, by convention, is defined to be zero for a wall-resolved portion (i.e., for such near-wall locations where the grid resolution, combined with the local shear stress, is considered sufficient for adopting a WRLES approach), conversely, it is set to one if the portion of the wall requires the wall model intervention. As pointed out in Fig. 19, the wall model intervention competes in about 50% of sampled occurrences for $x^* < -10$. This indicates that the incoming boundary layer's near-wall resolution permits the flow to be considered partly resolved, particularly for the most resolved arrangement. On the other hand, θ_{wm} values in the recirculation bubble area are close to zero, with a minimum at $x^* \approx -3.5$. Thus, the result enables us to assert that the model treats the recirculation bubble as a suitably resolved flow part. This finding is simply explained since the friction coefficient must vanish at the separation and reattachment bubble location. Thus, by decreasing the near-wall velocity gradients, near-wall resolution requirements drop. Finally, when $x^* > 0$, since near-wall resolutions are consistently above the WRLES threshold, θ_{WM} is steadily statistically equal to one, demonstrating that the wall model constantly operates across the whole ramp region.

4.4.3. Mean flow results discussion

After examining the instantaneous fields, we now investigate the system's average dynamics. Fig. 18 depicts the freestream-scaled ensemble-averaged velocity, $\tilde{u}^* = \tilde{u}/u_\infty$ (Figs. 18(a), 18(c), 18(e)) and the freestream scaled turbulent kinetic energy, $k^* = \widetilde{\rho u_i'' u_i''}/2q_\infty$ (Figs. 18(b), 18(d), 18(f)) fields around the ramp's leading edge as a function of the three mesh resolutions. As qualitatively observed while commenting on the instantaneous flow evolution, averaged velocity confirms that the ramp leading edge portion is covered by a recirculation bubble that spans from $x^* \approx -4$ up to $x^* \approx 1$. We also confirmed that adverse velocity events are detected on the average flow, a significant result for a WMLES computation that exploits

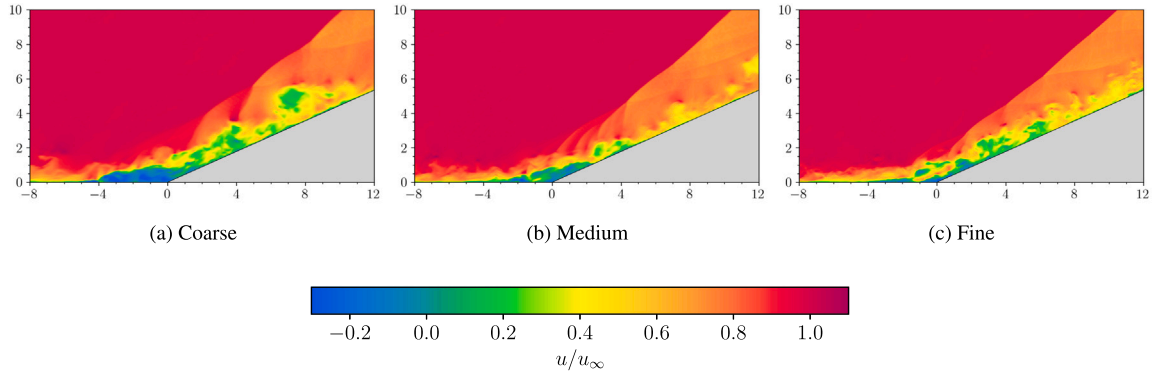

Fig. 17. Supersonic ramp freestream-scaled instantaneous u-velocity component contours for the three mesh configurations.

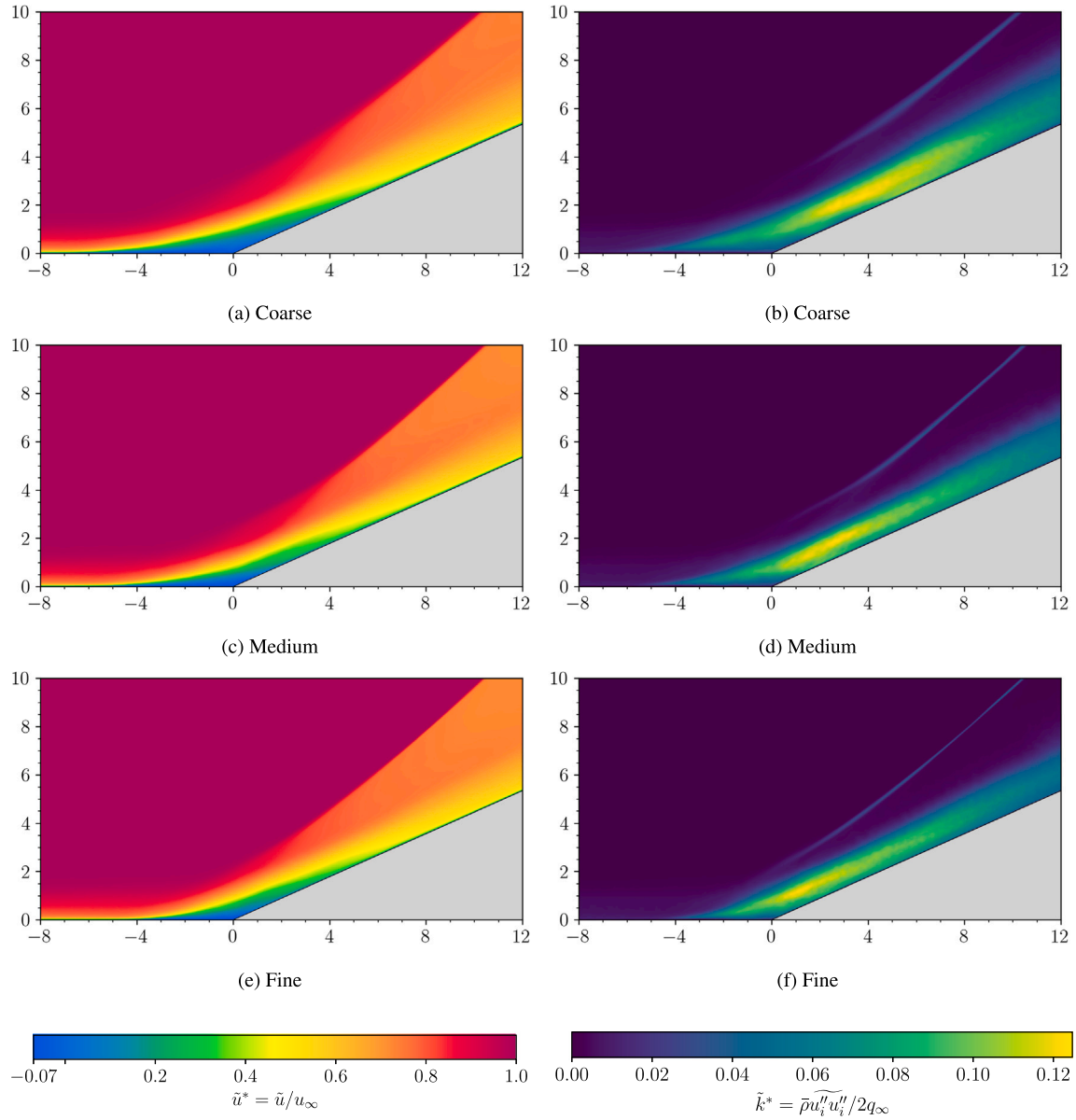

Fig. 18. Supersonic ramp freestream-scaled averaged u-velocity component (18(a), 18(c), 18(e)) and turbulent kinetic energy (18(b), 18(d), 18(f)) contours for the three mesh configurations.

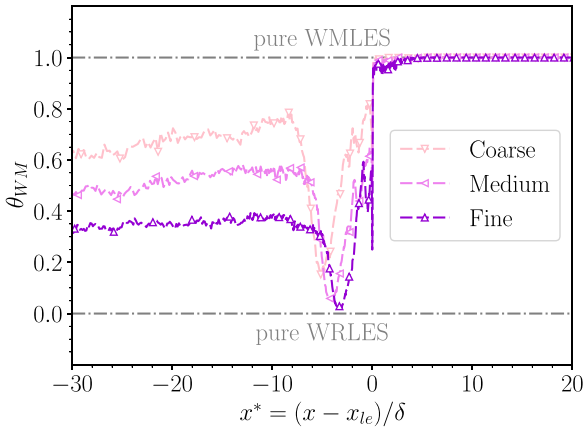

Fig. 19. Wall-modeled LES activation sensor as a function of the non-dimensional streamwise coordinate.

an equilibrium-based wall model. Eqs. (10), in fact, do not provide boundary layer solutions in partial recirculation conditions. Thus, the explanation of negative velocity occurrences has to be found in the adaptability of the current IBM+WMLES model, which can self-regulate the *effective viscosity* value concerning the assessment of the wall's local resolution. Indeed, based on the WMLES sensor distribution, we discovered that the bubble area is primarily treated as a wall-resolved portion, letting the model not rule out negative velocity gradients on the wall.

Average fields also provide information about the resolution effect. The coarse and the medium arrangements exhibit a λ-shock structure due to the junction of two shock waves at a triple point. The latter is clearly visible from the turbulent kinetic energy field, which shows how the primary shock wave trace keeps a compact behavior up to a specific location while grinding away as it progressively approaches the wall (Figs. 18(b), 18(d) and 18(f)). The λ-shock's rearmost branch, with low compression intensity, is mainly owing to the ramp-like effect caused by the recirculation bubble and has no physical meaning but is purely connected to the low mesh resolutions. On the other hand, the second branch is of a physical character and is caused by the geometric discontinuity. In the most resolved condition, the first branch tends to merge with the main shock, even though it is not wholly absorbed. The presence of the first branch is explained by three concurrent factors: (i) First and foremost, the low resolution provides turbulent viscosity values that tend to laminarize the recirculation zones, increasing their size; (ii) second, lower resolution tends to smear the primary shock, losing its strength while approaching the wall and making it unable to undermine the recirculating bubble from the wall; (iii) third, the wall model does not include any pressure gradient correction, and to correctly represent events of this kind, a comprehensive non-equilibrium model would be required. As a result, recirculating area and the region of intense turbulent kinetic value reduce in size while increasing the resolution. Similar findings have already been discussed by De Vanna et al. [89] in canonical shock-wave/boundary layer configurations.

Finally, to quantitatively trace the average near-wall dynamics and compare present model results with the reference DNS, Fig. 20 reports the freestream-scaled wall pressure, $\bar{p}^*_w = \bar{p}_w/p_\infty$, and the friction coefficient, $C_f = \tau_w/q_\infty$, distributions as a function of the non-dimensional streamwise coordinate and parametrically to the grid resolution. As seen from Fig. 20(a), as the resolution increases, the wall-pressure trace progressively matches the DNS reference by Priebe and Martín [88], and just a mild deviation is detected in the initial pressure rise. This is owing to the previously mentioned existence of a non-physical λ-shock structure that tends to anticipate ramp compression. Fig. 20(a) also depicts the theoretical wall pressure trend according to shock-expansion theory computations. Again, the current WMLES approach can wholly recover the inviscid solution when moving out from the shock wave/boundary layer interaction zone. Looking at Fig. 20(b), the friction coefficient trend also progressively recovers the DNS trend while increasing the mesh refinement. In particular, from such results, it can be concluded that the equilibrium-based boundary layer portions have achieved convergence. This is evident from the data collapsing over the flat-plate boundary layer in the inflowing region and the data collapse in the outflowing portion. Furthermore, the outflowing region convergence is mostly independent of the chosen resolution, letting us infer that the results obtained with the most refined mesh represent the convergence obtainable with the hybrid WR/WMLES model. According to the activation sensor distribution, θ_{WM}, increasing the resolution only leads to obtaining wall-resolved results exclusively in the upcoming boundary layer region. Conversely, the lack of convergence in the bubble area primarily stems from the adopted wall model rather than the proposed method. Using a non-equilibrium wall model would undoubtedly enhance the overall performance in this area. However, the intriguing result is that the current IBM+WMLES technique can recover adverse velocity gradient events, producing friction coefficient values that closely fit the DNS data in the bubble region. This is because the proposed method disables the wall model where the near-wall resolution meets the conditions expressed by Eq. (21) and uses a traditional wall-resolved strategy; thus, not ruling out negative velocity occurrences as would be the case of a standard wall model.

To conclude, the current IBM+WMLES technique systematically overestimates the bubble size compared to DNS data, with a separation point anticipated at about one δ upstream of the DNS location. Delayed boundary layer recovery along with the sloped surface is also systematically detected. A recirculating portion is observed, which is non-trivial in wall-modeled arrangements. In-equilibrium portions, instead, are accurately described, mostly independently of the grid resolution.

5. Conclusions

The paper proposes a novel LES method for analyzing complex wall flows as in engineering applications. In particular, we address high-Reynolds/high-Mach number flows by merging a well-established wall-modeled LES approach wealth discussed in previous literature [45,51,52,89] with an immersed boundary method. The overall approach generalizes the wall-modeling procedure to a non-conformal-grid geometrical environment.

The wall model is a distinct approach that involves increasing the turbulent parameters at the wall location to achieve the desired wall shear stress and heat flux. The method, in particular, does not rule out flow separations from the description of the near-wall dynamics and automatically reverts to a wall-resolved LES if the spatial resolution allows it. On the other hand, the adopted immersed boundary method represents a well-established sharp-interface approach already widely discussed in previous publications [36,38,90].

After discussing the numerical framework, the solver details, and the proposed immersed-boundary/wall-modeled LES algorithm characteristics, the paper includes multiple benchmarks and test cases to validate the proposed approach for engineering setups. In particular, ranging from low-Mach flow regimes within a turbulent channel and a pipe up to high Mach number flows associated with the boundary layer deployment over a flat plate and the shock-wave/boundary-layer interaction over a compression ramp configuration, the method is found to be able to head the time-dependent flow dynamics associated with each configuration. Such setups are selected as they have a wealth of DNS literature to compare with, but they are also revisited to a wholly immersed boundary logic in light of being fruitful combined with the proposed methodology. The tests demonstrate the model consistency against DNS reference, as well as the capacity of the model to be exploited as a predictive framework to address higher-Reynolds number flows presently out of current capacity concerning other scale-resolved methods, e.g., wall-resolved LES or DNS.

The method represents a promising strategy to compel with LES of complex aerodynamics flows at least for the following reasons:

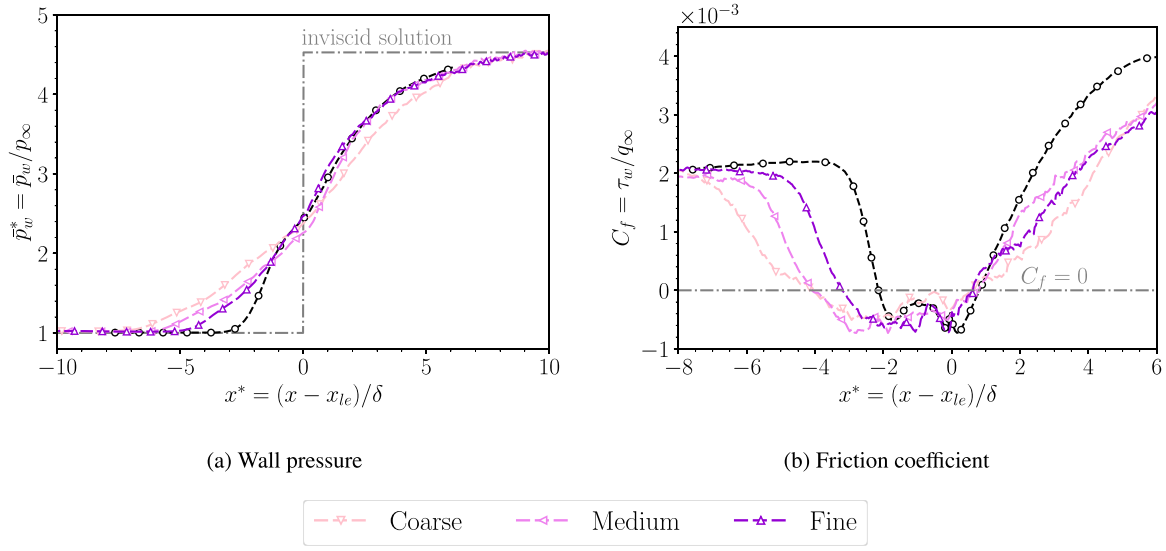

(a) Wall pressure

(b) Friction coefficient

Fig. 20. Wall pressure trace and friction coefficient distribution as a function of the streamwise coordinate. Present results (colors with triangles) are compared with DNS data by Priebe and Martín [88] (circles).

1. It simplifies the grid tuning procedure associated with the pre-processing effort.
2. It allows using accurate hybrid central/shock-capturing numerical schemes in a high-order finite difference discretization framework.
3. It reduces the computational effort associated with LES by decoupling the near-wall and the outer resolution requirements letting the model handle the near-wall dynamics.
4. It guarantees coupling the immersed boundary method in high-Reynolds/high-Mach conditions.
5. It minimizes the numerical viscosity injection, thus leaving the solely eddy-viscosity model to handle the subgrid-scale terms granting an accurate description of time-dependent flow features.
6. It allows using fully structured Cartesian grids that, combined with fully-explicit numerical methods, perfectly meet the demands of contemporary massive parallel computations on graphics processing units.

To conclude, the proposed approach stands as a promising path in accurately heading compressible aerodynamic problems over complex geometries, meeting many of the concurrent requirements that contemporary fluid dynamics poses for upcoming computations. Finally, the potential for future advancements is vast, given the method's purpose of simulating practical engineering configurations. Here is just a concise selection of possible extensions:

1. Extending the method to the treatment of completely three-dimensional complex geometries through the coding of an interface capable of pre-processing geometry in STL format. This fact will allow the use of the method and the solver for realistic engineering applications such as wings or aeroengine blades.
2. Another demanding task for the future concerns the improvement of the model for out-of-equilibrium effects associated with non-null wall pressure gradients.
3. Finally, a multiblock framework is required in order to be able to manage grid portions with very different resolutions.

CRediT authorship contribution statement

Francesco De Vanna: Conceptualization, Methodology, Software, Validation, Formal analysis, Investigation, Data curation, Writing – original draft, Writing – review & editing, Visualization. **Giacomo Baldan:** Software, Validation, Formal analysis, Investigation, Data curation, Writing – original draft, Writing – review & editing, Visualization. **Francesco Picano:** Writing – review & editing, Supervision. **Ernesto Benini:** Writing – review & editing, Supervision.

Declaration of competing interest

The authors declare that they have no known competing financial interests or personal relationships that could have appeared to influence the work reported in this paper.

Data availability

Data will be made available on request.

Acknowledgments

The authors acknowledge the "Consorzio Interuniversitario per il Calcolo Automatico" (CINECA) for guaranteeing us access to the Marconi100 supercomputer in the framework of the HP10BJK91V project under the ISCRA-B initiative. The authors also thank Matt Bettencourt, PhD from NVIDIA Corporation for the fruitful discussions about GPU architectures and porting issues.

References

[1] Chapman DR. Computational aerodynamics development and outlook. AIAA J 1979;17(12):1293–313. http://dx.doi.org/10.2514/3.61311.
[2] Choi H, Moin P. Grid-point requirements for large eddy simulation: Chapman's estimates revisited. Phys Fluids 2012;24(1):011702. http://dx.doi.org/10.1063/1.3676783.
[3] Spalart PR. Detached-eddy simulation. Annu Rev Fluid Mech 2009;41:181–202. http://dx.doi.org/10.1146/annurev.fluid.010908.165130.
[4] Piomelli U, Balaras E. Wall-layer models for large-eddy simulations. Annu Rev Fluid Mech 2002;34(1):349–74. http://dx.doi.org/10.1146/annurev.fluid.34.082901.144919.
[5] Bose ST, Park GI. Wall-modeled large-eddy simulation for complex turbulent flows. Annu Rev Fluid Mech 2018;50:535. http://dx.doi.org/10.1146/annurev-fluid-122316-045241.
[6] Cabot W, Moin P. Approximate wall boundary conditions in the large-eddy simulation of high Reynolds number flow. Flow Turbul Combust 2000;63(1):269–91. http://dx.doi.org/10.1023/A:1009958917113.
[7] Wang M, Moin P. Dynamic wall modeling for large-eddy simulation of complex turbulent flows. Phys Fluids 2002;14(7):2043–51. http://dx.doi.org/10.1063/1.1476668.

[8] Temmerman L, Leschziner MA, Mellen CP, Fröhlich J. Investigation of wall-function approximations and subgrid-scale models in large eddy simulation of separated flow in a channel with streamwise periodic constrictions. Int J Heat Fluid Flow 2003;24(2):157–80. http://dx.doi.org/10.1016/S0142-727X(02)00222-9.

[9] Kawai S, Larsson J. Wall-modeling in large eddy simulation: length scales, grid resolution, and accuracy. Phys Fluids 2012;24(1):015105. http://dx.doi.org/10.1063/1.3678331.

[10] Kawai S, Asada K. Wall-modeled large-eddy simulation of high Reynolds number flow around an airfoil near stall condition. Comput & Fluids 2013;85:105–13. http://dx.doi.org/10.1016/j.compfluid.2012.11.005.

[11] Bose ST, Moin P. A dynamic slip boundary condition for wall-modeled large-eddy simulation. Phys Fluids 2014;26(1):015104. http://dx.doi.org/10.1063/1.4849535.

[12] Bermejo-Moreno I, Campo L, Larsson J, Bodart J, Helmer D, Eaton JK. Confinement effects in shock wave/turbulent boundary layer interactions through wall-modelled large-eddy simulations. J Fluid Mech 2014;758:5–62. http://dx.doi.org/10.1017/jfm.2014.505.

[13] Park GI, Moin P. An improved dynamic non-equilibrium wall-model for large eddy simulation. Phys Fluids 2014;26(1):37–48. http://dx.doi.org/10.1063/1.4861069.

[14] Yang XI, Lv Y. A semi-locally scaled eddy viscosity formulation for LES wall models and flows at high speeds. Theor Comput Fluid Dyn 2018;32(5):617–27. http://dx.doi.org/10.1007/s00162-018-0471-3.

[15] Mettu BR, Subbareddy PK. Wall modeled LES of compressible flows at non-equilibrium conditions. In: 2018 fluid dynamics conference. 2018, p. 3405. http://dx.doi.org/10.2514/6.2018-3405.

[16] Suga K, Sakamoto T, Kuwata Y. Algebraic non-equilibrium wall-stress modeling for large eddy simulation based on analytical integration of the thin boundary-layer equation. Phys Fluids 2019;31(7):075109. http://dx.doi.org/10.1063/1.5099658.

[17] Larsson J, Kawai S, Bodart J, Bermejo-Moreno I. Large eddy simulation with modeled wall-stress: recent progress and future directions. Mech Eng Rev 2016;3(1):15–00418. http://dx.doi.org/10.1299/mer.15-00418.

[18] Peskin CS. Flow patterns around heart valves: a numerical method. J Comput Phys 1972;10(2):252–71. http://dx.doi.org/10.1016/0021-9991(72)90065-4.

[19] Fadlun E, Verzicco R, Orlandi P, Mohd-Yusof J. Combined immersed-boundary finite-difference methods for three-dimensional complex flow simulations. J Comput Phys 2000;161(1):35–60. http://dx.doi.org/10.1006/jcph.2000.6484.

[20] Iaccarino G, Verzicco R. Immersed boundary technique for turbulent flow simulations. Appl Mech Rev 2003;56(3):331–47. http://dx.doi.org/10.1115/1.1563627.

[21] Mittal R, Iaccarino G. Immersed boundary methods. Annu Rev Fluid Mech 2005;37:239–61. http://dx.doi.org/10.1146/annurev.fluid.37.061903.175743.

[22] Uhlmann M. An immersed boundary method with direct forcing for the simulation of particulate flows. J Comput Phys 2005;209(2):448–76. http://dx.doi.org/10.1016/j.jcp.2005.03.017.

[23] Eshghinejadfard A, Abdelsamie A, Hosseini SA, Thévenin D. Immersed boundary lattice Boltzmann simulation of turbulent channel flows in the presence of spherical particles. Int J Multiph Flow 2017;96:161–72. http://dx.doi.org/10.1016/j.ijmultiphaseflow.2017.07.011.

[24] Breugem WP. A second-order accurate immersed boundary method for fully resolved simulations of particle-laden flows. J Comput Phys 2012;231(13):4469–98. http://dx.doi.org/10.1016/j.jcp.2012.02.026.

[25] Kempe T, Fröhlich J. An improved immersed boundary method with direct forcing for the simulation of particle laden flows. J Comput Phys 2012;231(9):3663–84. http://dx.doi.org/10.1016/j.jcp.2012.01.021.

[26] Merlin C, Domingo P, Vervisch L. Immersed boundaries in large eddy simulation of compressible flows. Flow Turbul Combust 2013;90:29–68. http://dx.doi.org/10.1007/s10494-012-9421-0.

[27] Picano F, Breugem WP, Brandt L. Turbulent channel flow of dense suspensions of neutrally buoyant spheres. J Fluid Mech 2015;764:463–87. http://dx.doi.org/10.1017/jfm.2014.704.

[28] Schwarz S, Kempe T, Fröhlich J. A temporal discretization scheme to compute the motion of light particles in viscous flows by an immersed boundary method. J Comput Phys 2015. http://dx.doi.org/10.1016/j.jcp.2014.10.039.

[29] Luo K, Zhuang Z, Fan J, Haugen NEL. A ghost-cell immersed boundary method for simulations of heat transfer in compressible flows under different boundary conditions. Int J Heat Mass Transfer 2016;92:708–17. http://dx.doi.org/10.1016/j.ijheatmasstransfer.2015.09.024.

[30] Eshghinejadfard A, Thévenin D. Numerical simulation of heat transfer in particulate flows using a thermal immersed boundary lattice Boltzmann method. Int J Heat Fluid Flow 2016;60:31–46. http://dx.doi.org/10.1016/j.ijheatfluidflow.2016.04.002.

[31] Mittal R, Bhardwaj R. Immersed boundary methods for thermofluids problems. Annu Rev Heat Transf 2022;24. http://dx.doi.org/10.1615/AnnualRevHeatTransfer.2022041888.

[32] Piquet A, Roussel O, Hadjadj A. A comparative study of Brinkman penalization and direct-forcing immersed boundary methods for compressible viscous flows. Comput & Fluids 2016;136:272–84. http://dx.doi.org/10.1016/j.compfluid.2016.06.001.

[33] Bernardini M, Modesti D, Pirozzoli S. On the suitability of the immersed boundary method for the simulation of high-Reynolds-number separated turbulent flows. Comput & Fluids 2016;130:84–93. http://dx.doi.org/10.1016/j.compfluid.2016.02.018.

[34] Boukharfane R, Ribeiro FHE, Bouali Z, Mura A. A combined ghost-point-forcing/direct-forcing immersed boundary method (IBM) for compressible flow simulations. Comput & Fluids 2018;162:91–112. http://dx.doi.org/10.1016/j.compfluid.2017.11.018.

[35] Abdol Azis MH, Evrard F, van Wachem B. An immersed boundary method for flows with dense particle suspensions. Acta Mech 2019;230:485–515. http://dx.doi.org/10.1007/s00707-018-2296-y.

[36] De Vanna F, Picano F, Benini E. A sharp-interface immersed boundary method for moving objects in compressible viscous flows. Comput & Fluids 2020;201:104415. http://dx.doi.org/10.1016/j.compfluid.2019.104415.

[37] De Vanna F, Picano F, Benini E, Quinn MK. Large-eddy simulations of the unsteady behavior of a hypersonic intake at mach 5. AIAA J 2021;59(10):3859–72. http://dx.doi.org/10.2514/1.J060160.

[38] De Vanna F, Picano F, Benini E. Large-eddy-simulations of the unsteady behaviour of a mach 5 hypersonic intake. In: AIAA scitech 2021 forum. 2021, p. 0858. http://dx.doi.org/10.2514/6.2021-0858.

[39] Verzicco R. Immersed boundary methods: Historical perspective and future outlook. Annu Rev Fluid Mech 2023;55. http://dx.doi.org/10.1146/annurev-fluid-120720-022129.

[40] Cristallo A, Verzicco R. Combined immersed boundary/large-eddy-simulations of incompressible three dimensional complex flows. Flow Turbul Combust 2006;77:3–26. http://dx.doi.org/10.1007/s10494-006-9034-6.

[41] Roman F, Armenio V, Fröhlich J. A simple wall-layer model for large eddy simulation with immersed boundary method. Phys Fluids 2009;21(10). http://dx.doi.org/10.1063/1.3245294.

[42] Tamaki Y, Kawai S. Wall modeling for large-eddy simulation on non-body-conforming Cartesian grids. Phys Rev Fluids 2021;6(11):114603. http://dx.doi.org/10.1103/PhysRevFluids.6.114603.

[43] Krajnović S, Davidson L. Large-eddy simulation of the flow around a ground vehicle body. SAE technical paper, 2001, http://dx.doi.org/10.4271/2001-01-0702.

[44] Bae HJ, Lozano-Durán A. Effect of wall boundary conditions on a wall-modeled large-eddy simulation in a finite-difference framework. Fluids 2021;6(3):112. http://dx.doi.org/10.3390/fluids6030112.

[45] De Vanna F, Cogo M, Bernardini M, Picano F, Benini E. Unified wall-resolved and wall-modeled method for large-eddy simulations of compressible wall-bounded flows. Phys Rev Fluids 2021;6(3):034614. http://dx.doi.org/10.1103/PhysRevFluids.6.034614.

[46] De Vanna F, Avanzi F, Cogo M, Sandrin S, Bettencourt M, Picano F, et al. URANOS: A GPU accelerated Navier-Stokes solver for compressible wall-bounded flows. Comput Phys Comm 2023;287:108717. http://dx.doi.org/10.1016/j.cpc.2023.108717.

[47] Garnier E, Adams N, Sagaut P. Large eddy simulation for compressible flows. Springer Science & Business Media; 2009, http://dx.doi.org/10.1007/978-90-481-2819-8.

[48] Nicoud F, Ducros F. Subgrid-scale stress modelling based on the square of the velocity gradient tensor. Flow Turbul Combust 1999;62(3):183–200. http://dx.doi.org/10.1023/A:1009995426001.

[49] Chapman DR, Kuhn GD. The limiting behaviour of turbulence near a wall. J Fluid Mech 1986;170:265–92. http://dx.doi.org/10.1017/S0022112086000885.

[50] o'Rourke J. Computational geometry in C. Cambridge University Press; 1998.

[51] De Vanna F, Cogo M, Bernardini M, Picano F, Benini E. A straightforward strategy to unify WR/WMLES approaches for compressible wall-bounded flows. In: AIAA SCITECH 2022 forum. 2022, p. 0181. http://dx.doi.org/10.2514/6.2022-0181.

[52] De Vanna F, Michele C, Matteo B, Picano F, Benini E, et al. A wall-modeled/wall-resolved LES method for turbulent wall flows. In: ECCOMAS congress 2020. 2021, http://dx.doi.org/10.23967/wccm-eccomas.2020.045.

[53] Pirozzoli S. Generalized conservative approximations of split convective derivative operators. J Comput Phys 2010;229(19):7180–90. http://dx.doi.org/10.1016/j.jcp.2010.06.006.

[54] Fu L, Hu XY, Adams NA. A family of high-order targeted ENO schemes for compressible-fluid simulations. J Comput Phys 2016;305:333–59. http://dx.doi.org/10.1016/j.jcp.2015.10.037.

[55] Fu L, Hu XY, Adams NA. Targeted ENO schemes with tailored resolution property for hyperbolic conservation laws. J Comput Phys 2017;349:97–121. http://dx.doi.org/10.1016/j.jcp.2017.07.054.

[56] Fu L, Hu XY, Adams NA. A new class of adaptive high-order targeted ENO schemes for hyperbolic conservation laws. J Comput Phys 2018;374:724–51. http://dx.doi.org/10.1016/j.jcp.2018.07.043.

[57] Pirozzoli S, Bernardini M. Turbulence in supersonic boundary layers at moderate Reynolds number. J Fluid Mech 2011;688:120–68. http://dx.doi.org/10.1017/jfm.2011.368.

[58] Pirozzoli S. Stabilized non-dissipative approximations of Euler equations in generalized curvilinear coordinates. J Comput Phys 2011;230(8):2997–3014. http://dx.doi.org/10.1016/j.jcp.2011.01.001.

[59] Coppola G, Capuano F, Pirozzoli S, de Luca L. Numerically stable formulations of convective terms for turbulent compressible flows. J Comput Phys 2019;382:86–104. http://dx.doi.org/10.1016/j.jcp.2019.01.007.
[60] Modesti D, Pirozzoli S. Reynolds and mach number effects in compressible turbulent channel flow. Int J Heat Fluid Flow 2016;59:33–49. http://dx.doi.org/10.1016/j.ijheatfluidflow.2016.01.007.
[61] Modesti D, Pirozzoli S. Direct numerical simulation of supersonic pipe flow at moderate Reynolds number. Int J Heat Fluid Flow 2019;76:100–12. http://dx.doi.org/10.1016/j.ijheatfluidflow.2019.02.001.
[62] Jiang G-S, Shu CW. Efficient implementation of weighted ENO schemes. J Comput Phys 1996;126(1):202–28. http://dx.doi.org/10.1006/jcph.1996.0130.
[63] Cockburn B, Shu CW, Johnson C, Tadmor E, Shu CW. Essentially non-oscillatory and weighted essentially non-oscillatory schemes for hyperbolic conservation laws. Springer; 1998, http://dx.doi.org/10.1007/BFb0096355.
[64] Castro M, Costa B, Sun W. High order weighted essentially non-oscillatory WENO-Z schemes for hyperbolic conservation laws. J Comput Phys 2011;230(5):1766–92. http://dx.doi.org/10.1016/j.jcp.2010.11.028.
[65] Hamzehloo A, Lusher DJ, Laizet S, Sandham ND. On the performance of WENO/TENO schemes to resolve turbulence in DNS/LES of high-speed compressible flows. Internat J Numer Methods Fluids 2021;93(1):176–96. http://dx.doi.org/10.1002/fld.4879.
[66] Peng J, Liu S, Li S, Zhang K, Shen Y. An efficient targeted ENO scheme with local adaptive dissipation for compressible flow simulation. J Comput Phys 2021;425:109902. http://dx.doi.org/10.1016/j.jcp.2020.109902.
[67] Ducros F, Ferrand V, Nicoud F, Weber C, Darracq D, Gacherieu C, et al. Large-eddy simulation of the shock/turbulence interaction. J Comput Phys 1999;152(2):517–49. http://dx.doi.org/10.1006/jcph.1999.6238.
[68] De Vanna F, Baldan G, Picano F, Benini E. Effect of convective schemes in wall-resolved and wall-modeled LES of compressible wall turbulence. Comput & Fluids 2023;250:105710. http://dx.doi.org/10.1016/j.compfluid.2022.105710.
[69] De Vanna F, Benato A, Picano F, Benini E. High order conservative formulation of viscous terms for variable viscosity flows. Acta Mech 2021;232(6):2115–33. http://dx.doi.org/10.1007/s00707-021-02937-2.
[70] Gottlieb S, Shu CW. Total variation diminishing Runge-Kutta schemes. Math Comp 1998;67(221):73–85. http://dx.doi.org/10.1090/S0025-5718-98-00913-2.
[71] Reichardt H. Vollständige Darstellung der turbulenten Geschwindigkeitsverteilung in glatten Leitungen. J Appl Math Mech 1951;31(7):208–19. http://dx.doi.org/10.1002/zamm.19510310704.
[72] Georgiadis NJ, Rizzetta DP, Fureby C. Large-eddy simulation: current capabilities, recommended practices, and future research. AIAA J 2010;48(8):1772–84. http://dx.doi.org/10.2514/1.J050232.
[73] Vreman A, Kuerten JG. Statistics of spatial derivatives of velocity and pressure in turbulent channel flow. Phys Fluids 2014;26(8):085103. http://dx.doi.org/10.1063/1.4891624.
[74] Bernardini M, Pirozzoli S, Orlandi P. Velocity statistics in turbulent channel flow up to $Re_\tau = 4000$. J Fluid Mech 2014;742:171–91. http://dx.doi.org/10.1017/jfm.2013.674.
[75] Lee M, Moser RD. Direct numerical simulation of turbulent channel flow up to $Re_\tau \approx 5200$. J Fluid Mech 2015;774:395–415. http://dx.doi.org/10.1017/jfm.2015.268.
[76] Hoyas S, Oberlack M, Alcántara-Ávila F, Kraheberger SV, Laux J. Wall turbulence at high friction Reynolds numbers. Phys Rev Fluids 2022;7(1):014602. http://dx.doi.org/10.1103/PhysRevFluids.7.014602.
[77] Oberlack M, Hoyas S, Kraheberger SV, Alcántara-Ávila F, Laux J. Turbulence statistics of arbitrary moments of wall-bounded shear flows: A symmetry approach. Phys Rev Lett 2022;128(2):024502. http://dx.doi.org/10.1103/PhysRevLett.128.024502.
[78] Pope SB. Turbulent flows. Cambridge University Press; 2000.
[79] Henningson DS, Kim J. On turbulent spots in plane poiseuille flow. J Fluid Mech 1991;228:183–205. http://dx.doi.org/10.1017/S0022112091002677.
[80] Pirozzoli S, Romero J, Fatica M, Verzicco R, Orlandi P. One-point statistics for turbulent pipe flow up to $Re_\tau \approx 6000$. J Fluid Mech 2021;926. http://dx.doi.org/10.1017/jfm.2021.727.
[81] Nikuradse J. Stromungsgesetze in rauhen Rohren. VDI-Forschungsheft 1933;361:1.
[82] Poinsot T, Lelef S. Boundary conditions for direct simulations of compressible viscous flows. J Comput Phys 1992;101(1):104–29. http://dx.doi.org/10.1016/0021-9991(92)90227-p.
[83] Lodato G, Domingo P, Vervisch L. Three-dimensional boundary conditions for direct and large-eddy simulation of compressible viscous flows. J Comput Phys 2008;227(10):5105–43. http://dx.doi.org/10.1016/j.jcp.2008.01.038.
[84] Klein M, Sadiki A, Janicka J. A digital filter based generation of inflow data for spatially developing direct numerical or large eddy simulations. J Comput Phys 2003;186(2):652–65. http://dx.doi.org/10.1016/S0021-9991(03)00090-1.
[85] Kempf A, Wysocki S, Pettit M. An efficient, parallel low-storage implementation of Klein's turbulence generator for LES and DNS. Comput & Fluids 2012;60:58–60. http://dx.doi.org/10.1016/j.compfluid.2012.02.027.
[86] Musker A. Explicit expression for the smooth wall velocity distribution in a turbulent boundary layer. AIAA J 1979;17(6):655–7. http://dx.doi.org/10.2514/3.61193.
[87] White FM, Majdalani J. Viscous fluid flow, vol. 3. McGraw-Hill New York; 2006.
[88] Priebe S, Martín MP. Low-frequency unsteadiness in shock wave–turbulent boundary layer interaction. J Fluid Mech 2012;699:1–49. http://dx.doi.org/10.1017/jfm.2011.560.
[89] De Vanna F, Bernardini M, Picano F, Benini E. Wall-modeled LES of shock-wave/boundary layer interaction. Int J Heat Fluid Flow 2022;98:109071. http://dx.doi.org/10.1016/j.ijheatfluidflow.2022.109071.
[90] De Vanna F, Picano F, Benini E. An immersed boundary method for moving objects in compressible flows. In: Direct and large eddy simulation XII. Springer; 2020, p. 291–6. http://dx.doi.org/10.1007/978-3-030-42822-8_38.